



A single-ion-focused 393 nm laser for photon generation and qubit control

A master's thesis submitted to the faculty of mathematics, computer science
and physics, of the University of Innsbruck
in partial fulfillment of the requirements for the degree of

Master of Science (MSc)

carried out at the Institute of Experimental Physics under the supervision of
o.Univ.-Prof. Dr. Rainer Blatt,
Dr. Ben Lanyon

Presented by

Marco Canteri

Abstract

An ongoing project of building a three node quantum network is currently carried out at the university of Innsbruck with ion traps being the nodes of the network. To make entanglement between ions located in the three nodes, control over multiple ion-photon pairs is required. A laser beam has to be focused down to a single ion to generate photons out of individual ions in a string. In this thesis, an optical system is designed and built for focusing and steering the laser beam responsible for the photon generation process. Our experiment traps $^{40}\text{Ca}^+$ ions, the 393 nm laser triggers the generation of a photon via a cavity enhanced Raman process. The photon is emitted in a cavity and leaks out from one side. The designed setup comprises of an AOD, for steering the beam in the microsecond timescale, a set of lenses for expansion and control of the laser beam, and a custom objective for focusing the light on the ions. The system was designed and simulated with the software Zemax, and ultimately built on top of the existing experiment. We report two experiments that demonstrate the capabilities of the newly built setup. The first experiment generated photons out of a single ion in a string without exciting the ions not involved in the process. In the second experiment we applied a phase gate on a single ion-qubit, the phase shift induced is measured with a Ramsey interferometer. In addition to demonstrate single qubit manipulation capability, this experiment also allowed for a measure of the focus spot: 1.2-1.3 μm with an upper bound on the addressing error of 10^{-3} . These experiments are a stepping stone towards the realization of the aforementioned quantum network, the next key experiment is already ongoing, photons are produced from different ions creating a photon train. Afterwards, entanglement between ion and photon has to be achieved for each ion-photon pair.

Contents

1	Introduction	1
2	Theoretical framework	5
2.1	Quantum logic with trapped ions	5
2.1.1	Quantum computer and quantum gates	5
2.1.2	Ion qubits and laser-ion interactions	7
2.1.2.1	Three-level model	10
2.1.2.2	Dissipative processes	12
2.2	Quantum networking with trapped ions	12
2.2.1	General introduction	12
2.2.2	Cavity QED	13
2.2.3	Photon generation	14
2.3	Basics of ion trapping	15
2.3.1	Linear Paul trap	15
2.3.2	Ion strings	17
2.3.3	Doppler cooling	18
2.4	Laser beam	19
2.4.1	Gaussian beams	19
2.4.2	Beam steering via Acousto-optical Deflectors	22
2.5	Experiments model	24
2.5.1	Addressed qubit manipulation	24
2.5.2	Addressed photon generation	26
3	Conclusions and outlook	27
	References	28
	Appendix	34
A	AOD datasheet	35
B	Polarization characterization	39

Chapter 1

Introduction

A next step in technology advancement is represented by quantum technology, as it offers a radically new approach for the fields of computation, communication, simulation, and metrology [1]. For example, classical computers are limited in solving some particular problems that scale exponentially, and therefore a new approach is needed. Quantum computing can exploit particular features of quantum mechanics that have no classical counterparts, this allows for a speed up for a certain class of problems such as factorizing numbers [2], or searching in a database [3]. Moreover, simulating nature at its quantum level is a hard task for classical computer, while quantum computers are naturally prone to simulate quantum dynamics [4].

A collection of quantum computers interconnected via quantum channels forms a fully fledged quantum network [5]. However, for some quantum network applications, it is possible to relax the condition of having a universal quantum computer, a quantum device with a single qubit is enough as part of a functional quantum network with basic capabilities [6]. The concept of a quantum internet is to have a quantum channel along side with the classical channel, enabling the transmission of quantum information [6]. There are fundamental differences between a quantum channel and a classical link. Although the medium can be the same, such as optical fiber, a quantum channel must have additional abilities, such as distributing entanglement, or transmitting quantum states. Quantum networks have several applications: cryptographic wise they allow for more secure information transmission through Quantum Key Distribution [7], secure identification [8], blind quantum computation [9] and more [6]. Outside cryptography, quantum networks find applications in metrology: entanglement can be exploited to improve clock synchronization [10], and extend telescope's baselines [11]. Furthermore, quantum networks offer more efficient solutions to distributed system problems [12].

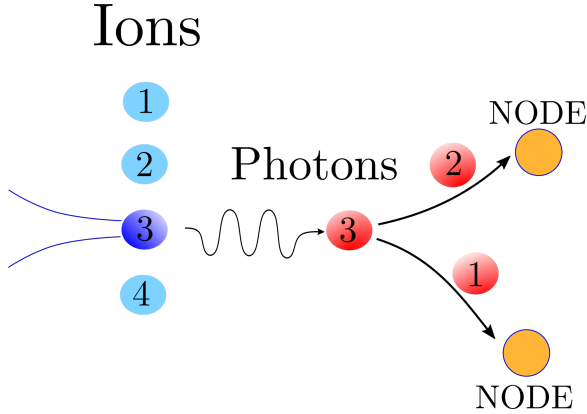
It is in this context that this thesis arises. Currently there is an ongoing project of building a three node quantum network between two buildings on the campus of the University of Innsbruck. The quantum nodes consist of ion traps: qubits are encoded in the electronic states of ions trapped in a Paul trap, while manipulation is done with laser pulses [13]. A 400 m optical fiber serves as link between the two buildings. This quantum network should have the ability to make entanglement with more than one other node in a network. This task requires the ability to connect multiple ions to multiple traveling direction-switchable photons. This is achieved with a single-ion-focused laser beam.

Photons are generated via a cavity enhanced Raman process [14], for which a 393 nm laser is used. When I started my master project, the 393 nm laser was shining on every

ion in the trap. In this case, if an ion string were to be loaded, the light would couple to every ion and there would be no control over the single ion-photon pair. The same 393 nm laser is also employed to perform ion-qubit manipulation by inducing an AC Stark shift on the qubit's ground state. A single-ion-focused laser allows to manipulate individual ion-qubits performing thus single qubit operations.

This thesis presents the development of an optical system that focuses the 393 nm laser beam on a single ion, and has the ability to steer the beam on a timescale of a few microseconds, which is the typical time for photon generation operations and ion-qubit operations. The setup is per se not complex, but the design is critical. Ions separation is typically around 5 micrometers in our system, so the light should be focused down to $1 - 2 \mu\text{m}$, at the limits of the optical elements involved. The steering part is achieved with an acousto-optical deflector (AOD), which deflects the laser light on microsecond timescales proportionally to the applied input frequency allowing to control remotely the beam pointing of the system. The AOD allows single ions in a string to be manipulated in two different ways:

SINGLE ION PHOTON GENERATION

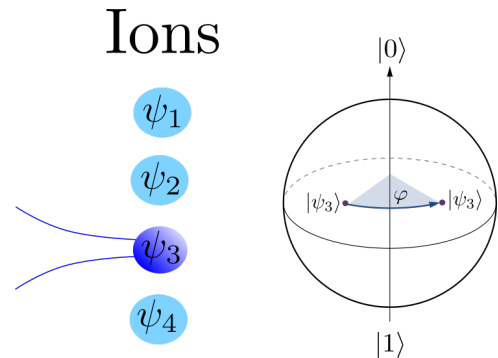


As illustrated in the sketch on the left, the idea is to generate photons from individual ions in a string and send them to the different nodes of the network. The laser beam is focused on a single ion, a laser pulse triggers the generation of a photon, the beam is then steered and focused on another ion to repeat the process. The approach we use is an ion-cavity system: the laser pulse triggers a cavity enhanced Raman process [14] that on resonance causes the emission of a photon from one ion into the cavity. The photon

subsequently leaks out from one of the cavity mirrors. In this thesis we set the goal of emitting photons from a particular ion without exciting any other ion in the string. This is a key step towards producing and controlling multiple photon-ion pairs.

SINGLE ION-QUBIT MANIPULATION

The same laser can perform quantum operations on the qubits encoded in the ions. Our goal is to manipulate the state of a single qubit without modifying the state of the others. Here the laser operates in a far-detuned regime, and induces an AC Stark shift on the $|0\rangle = |S_{j=1/2}, m_j = -1/2\rangle$ state of the ion-qubit implementing a phase gate [15]. In order to measure the AC Stark shift we perform a Ramsey interferometry experiment [16], where between the two $\pi/2$ pulses a detuned Stark pulse is introduced. This pulse shifts the relative phase of the qubit and therefore the amount of Stark shift can be inferred from the final qubit state.



The rest of this thesis is presented in the following way: Chapter 2 is devoted to the theoretical background necessary to understand the rest of the work. Here, the foundations of quantum computing and networking are laid down, along with the basic concepts of ion trapping and Gaussian laser beams; Chapter 3 presents the existing experimental setup, i.e. the already built and working blocks of the experiment where the setup designed in this thesis has been added; Chapter 4 is the core of the thesis, here the final design made with the software Zemax and simulations of different aspects of the project are introduced and presented; Chapter 5 contains all the experimental results obtained. It is divided in two parts: first, the setup was built on an optical table, here we had the freedom to test different key properties of the performance of the system and decide whether or not it was satisfactory. After having the certainty that the system can work as desired, the setup was transferred and aligned on the main experiment where limited access did not allow for easy performance testing. Here, we carried out two experiments that demonstrate the capability of the built system: to manipulate single qubits and generate photons from single ions. The description and discussion of these results are in the second part of chapter 5. Lastly, in Chapter 6 a conclusion with a summary and a future outlook is given.

Chapter 2

Theoretical framework

Quantum computing is based on a general framework that does not depend on the physical platform. In this chapter, important concepts such as qubits, and quantum operations are described from a theoretical point of view, before showing how we can realize them with trapped ions. The same goes with quantum networking, the concept and the realization can be treated separately and they will be described in this chapter. Furthermore, in this chapter we will take a look into Gaussian beams and their properties. Since that is the shape emitted by laser, it is important to understand their characteristics and how to manipulate them. Lastly, Acousto-optical interactions are introduced and studied to give an idea of how AODs work and how they can be used to steer a laser beam.

2.1 Quantum logic with trapped ions

2.1.1 Quantum computer and quantum gates

The concepts of quantum computing are borrowed and extended from classical computational. In the classical case, information is mostly represented in terms of binary digits, the so called bit, essentially mapping information to a base-2 number. Information processing is done with gates acting of those numbers. The idea of a quantum computer is still to encode information in a binary form, but due to the nature of quantum mechanics, a quantum bit (in short qubit) gains new features that can be exploited to perform different kind of operations.

A qubit is formally a normalized wave function that can be written as a superposition of two orthogonal states indicated usually with $|0\rangle$ and $|1\rangle$:

$$|\psi\rangle = \alpha |0\rangle + \beta |1\rangle, \quad (2.1.1)$$

where α, β are probability amplitudes, i.e. two complex numbers that satisfy the relationship $|\alpha|^2 + |\beta|^2 = 1$. A qubit can be in any linear combination, i.e. α and β . The outcome of measuring a qubit will give the value 0 with a probability of $|\alpha|^2$ and 1 with a probability of $|\beta|^2$.

Qubits also have a geometrical representation that can be useful. Equation (2.1.1) depends

on 4 real numbers, however since ψ is normalized, we can rewrite the expression as

$$|\psi\rangle = e^{i\gamma} \left(\cos \frac{\theta}{2} |0\rangle + e^{i\varphi} \sin \frac{\theta}{2} |1\rangle \right). \quad (2.1.2)$$

The global phase factor $e^{i\gamma}$ can be left out as it does not influence the measurement outcome, leaving only two real numbers: θ and φ . A qubit can therefore be represented geometrically with normalized spherical coordinates. The so called Bloch sphere is depicted in figure 2.1.1, every point on its surface represents a different state of the qubit. Here, qubit manipulation can be visualized as trajectories on the surface. The drawback of this representation is that it is limited to only one qubit, so it loses usefulness when dealing with multiple qubits.

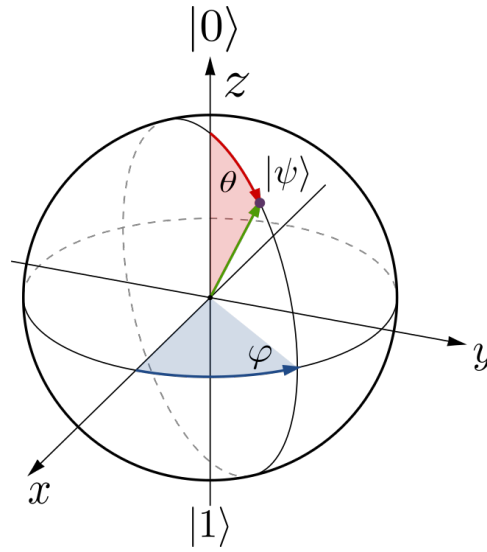


Figure 2.1.1: The Bloch sphere. The states $|0\rangle$ and $|1\rangle$ are at the poles of the sphere, every other point of the surface represents a superpositions of these states. A single qubit quantum gate can be seen as trajectory on the surface mapping one state to another.

An alternative way of dealing with qubits is via vectors and matrices. We can assign to the states $|0\rangle$ and $|1\rangle$ the following:

$$|0\rangle = \begin{pmatrix} 1 \\ 0 \end{pmatrix} \quad |1\rangle = \begin{pmatrix} 0 \\ 1 \end{pmatrix} \implies |\psi\rangle = \begin{pmatrix} \alpha \\ \beta \end{pmatrix}. \quad (2.1.3)$$

In this representation, single qubit rotations are calculated using 2×2 unitary matrices. These kind of operations are named *quantum gates* and they are the building blocks of quantum computing. Quantum algorithms can be written as a sequence of quantum gates. For a single qubit, any gate can be written as multiple combination of two operations, e.g. [17]

$$U_z(\Theta) = \begin{pmatrix} e^{-i\frac{\Theta}{2}} & 0 \\ 0 & e^{i\frac{\Theta}{2}} \end{pmatrix} \quad U_\varphi(\theta) = \begin{pmatrix} \cos \frac{\theta}{2} & -ie^{-i\varphi} \sin \frac{\theta}{2} \\ -ie^{i\varphi} \sin \frac{\theta}{2} & \cos \frac{\theta}{2} \end{pmatrix}. \quad (2.1.4)$$

These two matrices can be seen as two different rotations in the Bloch sphere, U_z is a rotation around the z axis by the angle Θ , while U_φ is a rotation around an axis located in the x - y plane. Important examples of single qubit gates are the Hadamard gate H ,

which creates a superposition of one qubit starting from the state $|0\rangle$, or $|1\rangle$, and the phase shift gate R_ϕ that shifts the phase:

$$H = \frac{1}{\sqrt{2}} \begin{pmatrix} 1 & 1 \\ 1 & -1 \end{pmatrix} \equiv U_{\varphi=\pi} \left(\frac{\pi}{2} \right) U_z(\pi) \quad R_\phi = \begin{pmatrix} 1 & 0 \\ 0 & e^{i\phi} \end{pmatrix} \equiv e^{i\varphi/2} U_z(\varphi). \quad (2.1.5)$$

Gates that involve N qubits are written as $2^N \times 2^N$ unitary matrices, a famous example is the controlled not (CNOT) gate

$$\text{CNOT} = \begin{pmatrix} 1 & 0 & 0 & 0 \\ 0 & 1 & 0 & 0 \\ 0 & 0 & 0 & 1 \\ 0 & 0 & 1 & 0 \end{pmatrix}. \quad (2.1.6)$$

It can be shown [15] that the examples of this section: H gate, phase gate, and CNOT gate form a universal set of quantum gates, i.e. a sequence of these gates approximates every other quantum gate.

2.1.2 Ion qubits and laser-ion interactions

Qubits can be encoded in any pair of orthogonal quantum states of a physical system. In figure 2.1.2 the level scheme of $^{40}\text{Ca}^+$ is presented. The states $|S_{1/2}\rangle$ and $|D_{5/2}\rangle$ are a common choice to encode a qubit. The ground state $|S_{1/2}\rangle$ represents the state $|0\rangle$ and the long lived (~ 1 s) excited state $|D_{5/2}\rangle$ will be $|1\rangle$. As these levels are directly connected by an electric-quadrupole transition at an optical wavelength (729 nm), this kind of qubit is often referred to as an optical qubit. Lasers provide a way to directly manipulate the population of these two levels and therefore to manipulate the state of the qubit.

The laser set up in this thesis is the 393 nm, which interacts via a dipole transition with the atomic ion, we model therefore the atom-light interactions as dipole interaction. In the case of a quadrupole interaction, the equations below still hold with the exception of the Rabi frequency, which will no longer depend linearly with the electric field. For a proper treatment of the quadrupole interaction see [18].

Consider the system in figure 2.1.3, where the states $|0\rangle$ and $|1\rangle$ are separated by a frequency ω_0 , while the laser is assumed to be monochromatic with frequency ω_l . The difference $\Delta = \omega_l - \omega_0$ is called detuning and we assume to be in the near resonant regime $\Delta \ll \omega_0$. The Hamiltonian of the atomic part can be written as:

$$H_a = \hbar\omega_0 |1\rangle \langle 1|, \quad (2.1.7)$$

where ω_0 is the frequency difference between the ground and excited state, the energy of the ground state has also been set to 0. The Hamiltonian of the interaction between the dipole atomic moment \mathbf{d} and the electric field of the laser can be written [19]

$$H_{int} = -\mathbf{d} \cdot \mathbf{E} \quad (2.1.8)$$

where the electric field will be treated classically and the dipole approximation is assumed. This means

$$\mathbf{E}(t) = \hat{\varepsilon} E_0 \cos(\omega_l t + \varphi) = \hat{\varepsilon} \frac{E_0}{2} (e^{-i(\omega_l t + \varphi)} + e^{i(\omega_l t + \varphi)}), \quad (2.1.9)$$

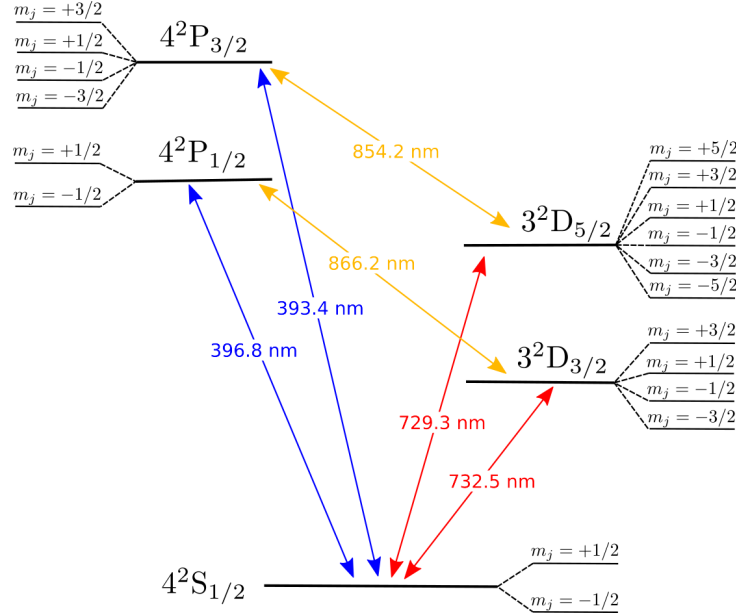


Figure 2.1.2: Level scheme of $^{40}\text{Ca}^+$. Detailed description is in section ?? . For quantum computing purposes, the chosen qubit transition is the long lived quadrupole transition $|S_{1/2}\rangle \rightarrow |D_{5/2}\rangle$ at 729nm.

where $\hat{\varepsilon}$ is the unit polarization vector. The next step is to work out the dipole operator, this can be done by applying the identity $|0\rangle\langle 0| + |1\rangle\langle 1|$ on both sides of d . Due to parity arguments [19], only the non diagonal terms are non-vanishing, giving

$$d = \langle 0|d|1\rangle (|0\rangle\langle 1| + |1\rangle\langle 0|) \equiv \langle 0|d|1\rangle (\sigma + \sigma^\dagger). \quad (2.1.10)$$

Combining the last three equations yields

$$H_{int} = -\langle 0|\hat{\varepsilon}\mathbf{d}|1\rangle \frac{E_0}{2} (\sigma e^{i(\omega_l t + \varphi)} + \sigma^\dagger e^{-i(\omega_l t + \varphi)} + \sigma e^{-i(\omega_l t + \varphi)} + \sigma^\dagger e^{i(\omega_l t + \varphi)}) \quad (2.1.11)$$

A rotating wave approximation is used now: in the interaction picture, the operator σ (σ^\dagger) evolves under the Hamiltonian H_a in time as $\tilde{\sigma} = e^{iH_a t/\hbar} \sigma e^{-iH_a t/\hbar} = \sigma e^{-i\omega_0 t}$ ($\tilde{\sigma}^\dagger = \sigma^\dagger e^{i\omega_0 t}$). Therefore, equation 2.1.11 in the interaction picture contains terms that oscillate as $\propto e^{\pm i(\omega_l - \omega_0)t}$, and $\propto e^{\pm i(\omega_l + \omega_0)t}$. We can drop the fast oscillating terms and keeping only those that depend on time as $\propto e^{\pm i(\omega_l - \omega_0)t}$. The validity of this approximation is given by the fact that ω and ω_0 are in the optical regime, thus they oscillate extremely fast and average to zero, the interesting slow dynamic is given only by their difference: the detuning. Going back in the Schrödinger picture yields the final form of the interaction Hamiltonian

$$H_{int} = \frac{\hbar\Omega}{2} (\sigma e^{i(\omega_l t + \varphi)} + \sigma^\dagger e^{-i(\omega_l t + \varphi)}), \quad (2.1.12)$$

where we defined the Rabi frequency $\Omega \equiv -\langle 0|\hat{\varepsilon}\mathbf{d}|1\rangle E_0/\hbar$. The Rabi frequency depends linearly with the applied electrical field and hence its square is proportional to the intensity of the laser $\Omega^2 \propto I$. To summarize, the total system Hamiltonian is

$$H = H_a + H_{int} = \hbar\omega_0 |1\rangle\langle 1| + \frac{\hbar\Omega}{2} (\sigma e^{i(\omega_l t + \varphi)} + \sigma^\dagger e^{-i(\omega_l t + \varphi)}). \quad (2.1.13)$$

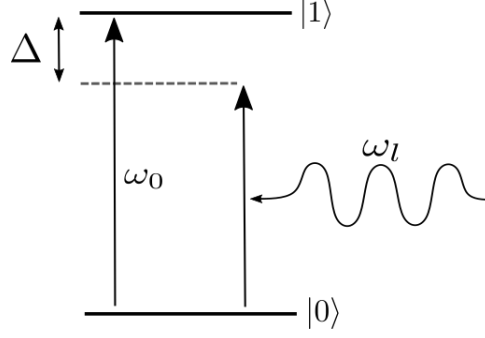


Figure 2.1.3: 2-level atom scheme, the ground and excited states are denoted as $|0\rangle$, and $|1\rangle$. ω_l is the laser frequency, which is detuned by $\Delta \equiv \omega_l - \omega_0$ from the transition frequency ω_0 .

To eliminate the time dependence, we can go in the rotating frame with the unitary transformation $U = e^{i\omega_l t|1\rangle\langle 1|}$, the Hamiltonian in this frame is

$$\tilde{H} = -\hbar\Delta |1\rangle\langle 1| + \frac{\hbar\Omega}{2}(e^{i\varphi}\sigma + e^{-i\varphi}\sigma^\dagger) \quad (2.1.14)$$

The time dependence is now gone, and the unitary evolution matrix can be calculated as

$$U(t) = \exp\left\{-\frac{i}{\hbar}\tilde{H}t\right\} = \begin{pmatrix} \cos\left(\frac{\tilde{\Omega}t}{2}\right) + i\frac{\Delta}{\tilde{\Omega}}\sin\left(\frac{\tilde{\Omega}t}{2}\right) & -ie^{i\varphi}\frac{\Omega}{\tilde{\Omega}}\sin\left(\frac{\tilde{\Omega}t}{2}\right) \\ -ie^{-i\varphi}\frac{\Omega}{\tilde{\Omega}}\sin\left(\frac{\tilde{\Omega}t}{2}\right) & \cos\left(\frac{\tilde{\Omega}t}{2}\right) - i\frac{\Delta}{\tilde{\Omega}}\sin\left(\frac{\tilde{\Omega}t}{2}\right) \end{pmatrix}. \quad (2.1.15)$$

Where $\tilde{\Omega} = \sqrt{\Delta^2 + \Omega^2}$ is the generalized Rabi frequency. In the case of zero detuning ($\Delta = 0$) the matrix is the same as equation (2.1.4), thus a resonant laser pulse implements the qubit rotation $U_\varphi(\theta)$.

As an example, let us take the atom in the ground state $|\psi\rangle = |0\rangle$ and apply the unitary evolution (2.1.15). The probability to be in the excited state becomes

$$\mathbb{P}\{|1\rangle\}(t) = |\langle 1|U(t)|0\rangle|^2 = \frac{\Omega^2}{\Omega^2 + \Delta^2} \sin^2\left(\frac{\tilde{\Omega}t}{2}\right) \quad (2.1.16)$$

This equation is plotted in figure 2.1.4. For $\Delta = 0$, we get a cosine behaviour, the so called Rabi oscillations. The probability amplitude for the electron, under continuous drive by a laser, will oscillate between the ground and excited state at a frequency $\Omega/2$. Detuning damps the amplitude of such oscillations and increases the oscillation frequency. Rabi oscillations are an important tool in quantum information, laser pulses can prepare the state of the qubit in any superposition, e.g. starting in the $|0\rangle$ state, a $\pi/2$ pulse ($\Omega t = \pi/2$ and phase $\varphi = 0$) will result in the state $(|0\rangle - i|1\rangle)/\sqrt{2}$, with a π pulse ($\Omega t = \pi$, $\varphi = \pi$) the population is completely transferred to another level $|0\rangle \rightarrow |1\rangle$. These pulses can be used to implement e.g. the Hadamard gate of equation (2.1.5).

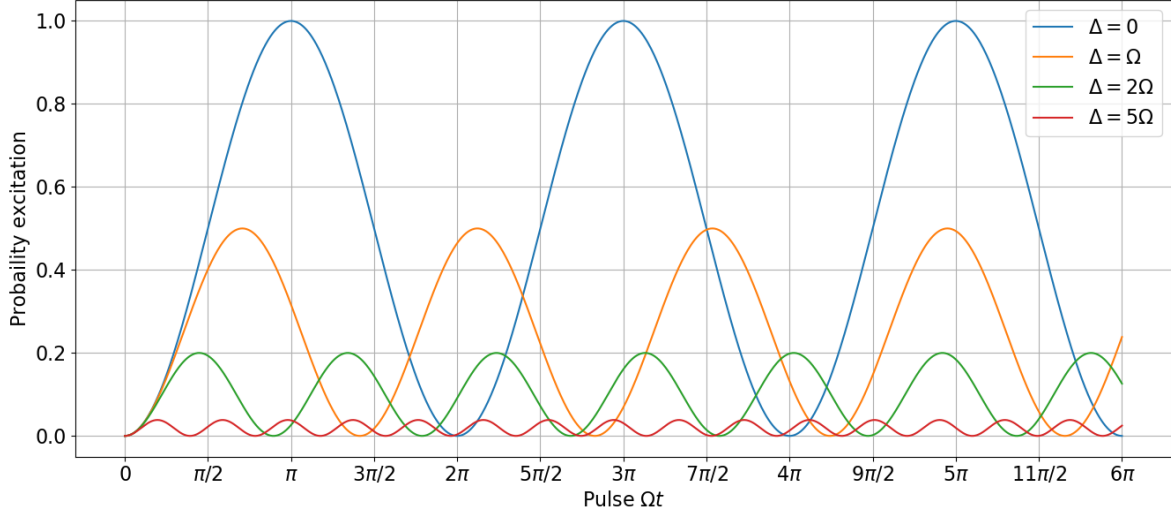


Figure 2.1.4: Rabi flops for different detunings Δ , starting from the $|0\rangle$ state.

As the light is detuned from the transition, Rabi oscillations are suppressed: the amplitude is reduced by a factor of 0.5 already with $\Delta = \Omega$, while a factor of 10 in reduction is achieved with a detuning of $\Delta = 5\Omega$. However, another effect occurs in the off-resonant regime, the energy levels are shifted. The shift δ can be calculated by finding the eigenvalues of the Hamiltonian (2.1.14), which can be written in matrix form and diagonalized. We find that there are two eigenstates $|+\rangle$ and $|-\rangle$ called dressed states with eigenvalues

$$E_{\pm} = -\frac{\hbar\Delta}{2} \pm \frac{\hbar}{2}\sqrt{\Delta^2 + \Omega^2}. \quad (2.1.17)$$

In the limit $\Delta \gg \Omega$, dressed states tend to the bare states $|+\rangle \rightarrow |1\rangle$, $|-\rangle \rightarrow |0\rangle$, and the energies become

$$E_{\pm} \rightarrow -\frac{\hbar\Omega}{2} \pm \frac{\hbar\Omega}{2} \pm \frac{\hbar\Omega^2}{4\Delta} \implies \delta = \pm \frac{\Omega^2}{4\Delta}. \quad (2.1.18)$$

The effective Hamiltonian for the off-resonant regime can be derived following a Markovian approximation [20]

$$H_{AC} = \frac{1}{\hbar\Delta}[\sigma, \sigma^\dagger] = \frac{\hbar\delta}{2}\sigma_z \quad (2.1.19)$$

The corresponding evolution is

$$U(t) = \exp\left\{-\frac{i}{\hbar}H_{AC}t\right\} = \begin{pmatrix} \exp\{i\frac{\delta}{2}t\} & 0 \\ 0 & \exp\{i\frac{\delta}{2}t\} \end{pmatrix}. \quad (2.1.20)$$

This matrix implements the quantum gate $U_z(\Theta)$ from equation (2.1.4).

2.1.2.1 Three-level model

We extend our model to a 3 level Λ type atom driven by two lasers, which closer resemble the real experimental situation in the experiments in this thesis. The model contains new effects that explain photon generation and qubit gates. In particular, stimulated Raman transition will be discussed, and we will show how, under certain conditions, the system can be approximated as an effective 2 level atom. The system is depicted in figure 2.1.5,

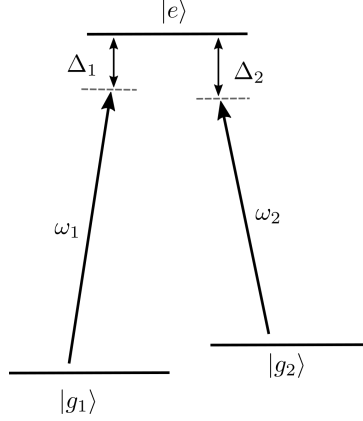


Figure 2.1.5: 3 level atom model. Two long lived ground states $|g_1\rangle$, $|g_2\rangle$ couple to an excited level $|e\rangle$ through two lasers of frequencies ω_1 , ω_2 detuned respectively Δ_1 , Δ_2 from the transitions.

two ground states $|g_1\rangle$ and $|g_2\rangle$ are present together with a common excited state $|e\rangle$. Two different lasers ω_1, ω_2 drive the transition $|g_1\rangle \rightarrow |e\rangle$ and $|g_2\rangle \rightarrow |e\rangle$, where the atomic frequencies are ω_{01} , and ω_{02} respectively. Detunings are defined as $\Delta_1 = \omega_1 - \omega_{01}$ and $\Delta_2 = \omega_2 - \omega_{02}$. In the case of calcium, the ground states are $|S_{1/2}\rangle$, and $|D_{5/2}\rangle$. This is the qubit transition, and it is long lived (~ 1 s), such that any spontaneous emission from D to S can be neglected. The excited level is $|P_{3/2}\rangle$ which can decay into both ground states with branch ratio of 94% from $P \rightarrow S$ (~ 7.4 ns) and 5.3% from $P \rightarrow D \sim 101$ ns), we neglect decay to the $|D_{3/2}\rangle$ state.

Following the approach of [19], the bare atom Hamiltonian is

$$H_a = -\hbar\omega_{01} |g_1\rangle \langle g_1| - \hbar\omega_{02} |g_2\rangle \langle g_2|, \quad (2.1.21)$$

with the convention of setting the excited level energy to 0. The electric field is now the sum of the two laser fields

$$\mathbf{E}(t) = \varepsilon_{01} E_{01} \cos(\omega_1 t + \varphi_1) + \varepsilon_{02} E_{02} \cos(\omega_2 t + \varphi_2). \quad (2.1.22)$$

As in section 2.1.2, we then consider a dipole interaction, make the dipole approximation and a rotating wave approximation. Finally, the full final Hamiltonian in the rotating frame is

$$H = \hbar\Delta_1 |g_1\rangle \langle g_1| + \hbar\Delta_2 |g_2\rangle \langle g_2| + \frac{\hbar\Omega_1}{2} \left(\sigma_1 e^{i\varphi_1} + \sigma_1^\dagger e^{-i\varphi_1} \right) + \frac{\hbar\Omega_2}{2} \left(\sigma_2 e^{i\varphi_2} + \sigma_2^\dagger e^{-i\varphi_2} \right), \quad (2.1.23)$$

where $\Omega_i = -\frac{\langle g_i | \varepsilon_i \cdot \mathbf{d} | e \rangle E_i}{\hbar}$, and $\sigma_i = |g_i\rangle \langle e|$. Under certain conditions, this Hamiltonian describes a Raman process, where state population is transferred coherently between $|g_1\rangle$ and $|g_2\rangle$. Specifically, the Raman conditions are: equal detunings $\Delta_1 = \Delta_2 \equiv \Delta$ (Raman resonance), and $\Delta \gg \Omega_1, \Omega_2$. Intuitively, this corresponds to the situation where the difference of the two driving frequencies $(\omega_1 - \omega_2)$ is equal to the frequency splitting between $|g_1\rangle$, and $|g_2\rangle$.

Following [21] it can be shown that, under the previous conditions, the Raman process leads to an effective coupling directly between the two ground states. The effective Rabi

frequency of the coherent population transfer $|g_1\rangle \rightarrow |g_2\rangle$ is [19]

$$\Omega_{eff} = \frac{\Omega_1 \Omega_2}{2\Delta}. \quad (2.1.24)$$

2.1.2.2 Dissipative processes

In our experiments spontaneous emission can play a role as the condition $\Delta \gg \Omega_1, \Omega_2$ is only partially fulfilled. In this section therefore, we present a quantitative overview of spontaneous scattering as a function of detuning and Rabi frequency of each laser. In general, dissipative processes do not follow a Hermitian evolution, hence their mathematical description is done heuristically by adding terms in the Heisenberg equation

$$\frac{d\rho}{dt} = \frac{1}{i\hbar}[H, \rho] + \mathcal{L}(\rho). \quad (2.1.25)$$

This equation is usually referred to as master equation in Lindblad form, where ρ is the density matrix of the system. The superoperator $\mathcal{L}(\rho)$ contains phenomena not included in the Hamiltonian. For spontaneous emission, the form of $\mathcal{L}(\rho)$ is [22]

$$\mathcal{L}(\rho) = \frac{\Gamma}{2}(2\sigma\rho\sigma^\dagger - \sigma^\dagger\sigma\rho - \rho\sigma^\dagger\sigma), \quad (2.1.26)$$

where Γ is the spontaneous emission rate. For the three level atom, in the effective 2 level system picture, the spontaneous emission is modified as [21]

$$\Gamma_{eff} = \left(\frac{\Omega_1}{2\Delta_1}\right)^2 \cdot \Gamma. \quad (2.1.27)$$

The ratio between Γ_{eff} and the AC Stark shift (2.1.18) $\delta/\Gamma_{eff} \propto \Delta$ dictates which effect is dominant, i.e. by increasing the detuning, the effective rate of spontaneous scattering can be reduced in favor of the AC Stark shift. This regime can be used to implement a phase gate where the qubit is encoded in the $|g_1\rangle \rightarrow |g_2\rangle$ transition and the phase of $|g_1\rangle$ is manipulated by Stark shifting the transition $|g_1\rangle \rightarrow |e\rangle$. In the experiment of section ??, we implement this gate on a single ion in a string.

2.2 Quantum networking with trapped ions

2.2.1 General introduction

A quantum network is a collection of quantum processors, referred to as nodes, interconnected with quantum channels, referred to as links. Nodes are used for processing and storing quantum information, while links for quantum information distribution [5]. Applications of quantum networks are several: secure communication with Quantum Key Distribution, clock synchronization, efficient solutions to distributed system problems, and more [6].

Links are typically realized with traveling photons, either in free-space [23] or in optical fibers. Nodes can be realized using different physical systems: trapped ions [24], neutral atoms [25], atomic ensembles [5]. Nodes and links are connected through an interface

that converts a stationary qubit in a node to a flying qubit over the network. In the next section we will explore how such an interface can be realized by placing an ion-qubit in an optical cavity.

Faithful transmission of quantum states over long distances can be a daunting problem as quantum information cannot be cloned [26] and noisy channels can destroy the delicate nature of qubits. Quantum repeaters have been designed [27] to circumvent these problems through a series of protocols which include entanglement purification, a form of error correction [28]. Once entanglement has been established between nodes, other network functionalities become available, like for instance teleportation [29]. Entanglement generation, and quantum repeaters are just some examples of the fundamental steps necessary for building a quantum network, for a more in depth review look at [6].

2.2.2 Cavity QED

A single trapped ion is a single photon source and those photons can be collected either with a lens [24], refocused with mirrors [30] or with optical cavities [31]. Photon collection from ions using an optical cavity is a powerful approach, that will now be introduced in detail. A cavity placed around ions improves the efficiency of photon collection as the probability of a photon to be emitted in the cavity mode is enhanced with respect to emitting in free space [32].

In this section a simple model of a two-level system in a cavity is described following the approach of [19]. We described the cavity electric field as quantized, with a, a^\dagger the creation and annihilation operators of a single photon in the cavity mode, respectively. The quantized electric field assumes the form of

$$\mathbf{E} = A(\mathbf{f}(\mathbf{r})a + \mathbf{f}^*(\mathbf{r})a^\dagger) \quad (2.2.1)$$

where A is an amplitude, and $\mathbf{f}(\mathbf{r})$ is the spatial mode profile. The interaction between the dipole moment of a two-level atom and the cavity field is in the dipole form

$$H_{int} = -\mathbf{d} \cdot \mathbf{E} = \hbar g(\sigma a^\dagger + \sigma^\dagger a), \quad (2.2.2)$$

where $g = A \langle 0|\mathbf{d}|1\rangle \cdot \mathbf{f}(\mathbf{r})$ is called the cavity coupling constant, it is analogous to the Rabi frequency. An important dependence of g can be found by considering that $f(r)$ is inversely proportional to the volume of the cavity V , i.e.

$$g \propto \langle 0|\mathbf{d}|1\rangle \sqrt{\frac{\omega}{2\varepsilon_0\hbar V}}. \quad (2.2.3)$$

The coupling therefore increases with decreasing cavity volume.

The total system Hamiltonian includes also the atomic part, and the free evolution of the cavity single mode field, it takes the name of Jaynes-Cummings Hamiltonian and it is written as [33]

$$H = \hbar\omega_0 |1\rangle \langle 1| + \hbar\omega a^\dagger a + \hbar g(\sigma a^\dagger + \sigma^\dagger a). \quad (2.2.4)$$

We are interested in comparing the coherent process in (2.2.4) with: spontaneous emission in a free space field mode, and decay in one cavity mode and out of the cavity. The first is quantified with the decay rate $\Gamma = 2\gamma$, while the latter is characterized by the decay rate κ (half width half maximum). The decay rate κ depends exclusively on the cavity

parameters as [34]

$$\kappa = \frac{c\pi}{FL}, \quad (2.2.5)$$

where F is the cavity finesse, and L the length.

2.2.3 Photon generation

In our experiments, photons are generated from an ion-cavity system. Photons generation involves three levels and occurs via the Raman process described in section 2.1.2.1. However, here the second laser is replaced by the vacuum electric field of the cavity in a process known as cavity-mediated Raman Process (CMRP) [14]. In Figure 2.2.1 the relevant calcium levels for the CMRP are displayed. A possible choice for the three levels is

$$|S_{1/2}, -1/2\rangle \rightarrow |P_{3/2}, -3/2\rangle \rightarrow |D_{5/2}, -5/2\rangle. \quad (2.2.6)$$

In this case the transitions strengths, i.e. the projection of the laser polarization onto the dipole moment, and the same projection onto the cavity axis are maximized over all other choices of transitions for the CMRP [14]. A single laser pulse with strength Ω couples the $S_{1/2}$ level to the $P_{3/2}$ level, which is coupled to the $D_{5/2}$ via the vacuum mode of the cavity. Therefore, the electron state is transferred from the state $|S_{1/2}\rangle \rightarrow |D_{5/2}\rangle$ by absorbing a laser photon and emitting a photon into the cavity. The final state is therefore $|D_{5/2}\rangle |1\rangle$, where $|1\rangle$ indicates one photon in the cavity. Afterwards, the photon leaves the cavity leaving the system in the $|D_{5/2}\rangle |0\rangle$ state. The effective Rabi frequency (2.1.24) of the population transfer is modified as [35]

$$\Omega_{eff} = \frac{\Omega g}{\Delta}, \quad (2.2.7)$$

where the Rabi frequency of the second laser is now replaced by the atom cavity coupling g . The Raman resonance appears when the detuning Δ of the laser and the cavity are the same. The effective spontaneous decay rate from this level is from equation (2.1.27)

$$\Gamma_{eff} = \left(\frac{\Omega}{2\Delta} \right)^2 \Gamma \quad (2.2.8)$$

The effective Rabi frequency Ω_{eff} and the effective spontaneous decay Γ_{eff} are competitive effects and the ratio of the two depends on the detuning $\Omega_{eff}/\Gamma_{eff} \propto \Delta/\Omega$. It is therefore possible to reduce spontaneous emission effects if the detuning is large enough.

In our experiment the designed cavity is near concentric with a length of $L = 19.9$ mm. The maximum g factor achievable with this geometry is $g_{max} = 2\pi \times 1.53$ MHz, while the decay rate is $\kappa = 2\pi \times 70$ kHz. More information on our cavity can be found in [36] and in the upcoming thesis of J. Schupp. Typical numbers in our experiment for the CMRP are $\Omega = 2\pi \times 40$ MHz, detuning $\Delta = 2\pi \times 400$ MHz, $g = 2\pi \times 1$ MHz, and from table ??, $\Gamma = 2\pi \times 21.4$ MHz. With these conditions we have

$$\Omega_{eff} \sim 2\pi \times 100 \text{ kHz} > \Gamma_{eff} \sim 2\pi \times 53 \text{ kHz}.$$

The regime we work in is thus $2\kappa > \Omega_{eff} > \Gamma_{eff}$. In section ??, we use the single-ion focused Raman laser, developed in this thesis, to implement the CMRP on a single ion in a string.

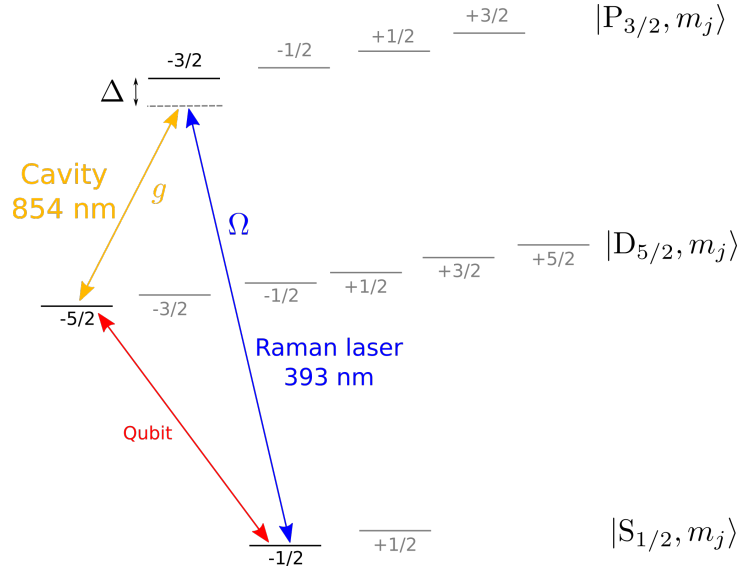


Figure 2.2.1: Displayed is the Zeeman structure of the relevant manifolds of calcium for the cavity-mediated Raman process. Here only one choice for the Zeeman level is depicted, but other are also possible. If the cavity and the Raman laser have the same detuning Δ , an electron in the ground state $|S_{1/2}\rangle$ absorbs a 393 nm photon and ends in the $|D_{5/2}\rangle$ state after emitting a 854 nm photon in the cavity.

2.3 Basics of ion trapping

2.3.1 Linear Paul trap

Ions are charged, therefore electric fields can be used to control and trap them. In order to achieve confinement in 3 dimensions, a potential $\phi(x, y, z)$ with minima in all directions is needed. However, it follows directly from Maxwell's equations $\nabla^2\phi = 0$ that the potential must be antitrapping at least in one direction. There are two workarounds for this problem: the first one introduces magnetic fields to trap particles in some directions, this takes the name of Penning trap [37]. The second solution is the so called Paul trap, and it is what we are going to describe in this section. The idea is to introduce a time varying potential, such that the antitrapping direction is constantly switching between two different dimensions. The particles will therefore experience an effective confinement in all directions if the switching is fast compared to the time it takes the particle to respond. The shape of the trap can be adapted to load more ions in different geometries. In our work we utilize a linear Paul trap, which is elongated in one direction. The confinement in this direction is weaker and thus loaded ions will align in a single long string. This kind of trap is depicted in figure 2.3.1. The confinement in the $x - y$ plane is provided by 4 electrodes, two of which are grounded and the other two are connected to a radio frequency source. This design is similar to a mass filter, with the difference of additional endcaps electrodes in the z direction that plug the trap and confine also in the axial direction.

The potential inside the trap can be described for the $x - y$ plan independently from the

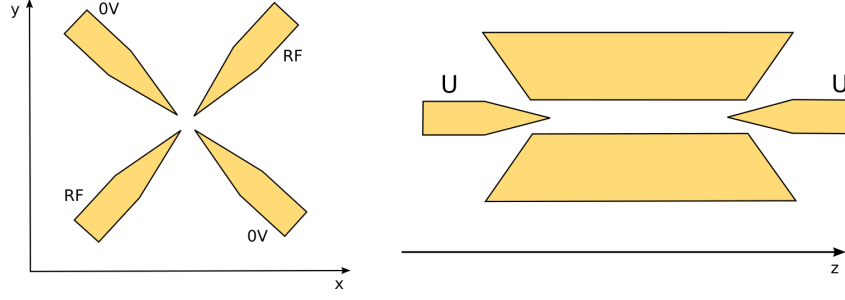


Figure 2.3.1: A linear Paul trap. U is the voltage applied to the electrodes trapping in the z direction, while in the $x - y$ plane trapping is achieved with a radio frequency signal.

z direction. In the case of a linear Paul trap the radial potential is [38]:

$$\phi = \frac{\Phi_0}{2r_0^2} (x^2 - y^2), \quad (2.3.1)$$

where r_0 is the distance from the center of the trap to the electrodes. The amplitude consists of a static part U_0 and a dynamical one $\Phi_0 = U_0 + V \cos(\Omega_{RF}t)$. The study of the particle's motion with mass m and charge e inside the trap can be done with classical physics, Newton's second law in this case is

$$m\ddot{x} = -q \frac{\partial \phi}{\partial x} = -\frac{ex}{r_0^2} (U_0 + V \cos(\Omega_{RF}t)), \quad (2.3.2)$$

and similarly for \ddot{y} . This equation can be written in the form of Mathieu equation [39] by defining two parameters:

$$a_x = \frac{4eU_0}{\Omega_{RF}^2 r_0^2 m}, \quad q_x = \frac{2eV}{\Omega_{RF}^2 r_0^2 m} \implies \ddot{x} + \frac{\Omega_{RF}^2}{4} (a_x + 2q_x \cos(\Omega_{RF}t)) x = 0 \quad (2.3.3)$$

and with a change of variable $\tau = \frac{\Omega_{RF}t}{2}$ we end up with

$$\frac{\partial^2 x}{\partial \tau^2} + (a_x + 2q_x \cos(2\tau)) x = 0 \quad (2.3.4)$$

This kind of equations have stable solutions that can be found in a recursive way with Floquet theorem [40]. In the limit $a_x \ll q_x \ll 1$, solutions to (2.3.4) are found to be

$$x(t) = x_0 \cos(\omega_x t + \phi_x) \left[1 + \frac{q_x}{2} \cos(\Omega_{RF}t) \right]. \quad (2.3.5)$$

Here, we recognize a slowly varying oscillation ω_x , referred to as *secular motion*, with amplitude modulated by a faster oscillation Ω_{RF} , called *micromotion*. The approximation, named secular, is valid only in the case $\omega_x \ll \Omega_{RF}$. The frequency ω_x is given in the solution as

$$\omega_x = \frac{\Omega_{RF}}{2} \sqrt{a_x + \frac{q_x^2}{2}}. \quad (2.3.6)$$

By imposing real solutions to (2.3.6), the stability diagram of the trap can be found [38]. The other spatial dimension can be treated in the same way and the results are the same. Confinement in the axial direction z is purposely weaker, and ions will align in this

direction. Two electrodes with constant potential U are present, they create a harmonic potential

$$V = \frac{1}{2}m\omega_z^2 z^2, \quad (2.3.7)$$

where ω_z is the axial trap frequency. In the case of a string of ions, mutual repulsions must also be included, in the next section we will consider this case.

2.3.2 Ion strings

For the goals of this thesis, we are interested in the separation between N ions loaded in the trap. This will give us an idea of how narrowly the beam should be focused and will set an appropriate problem spatial scale.

Let us consider the z direction where the ions are more weakly confined such that they form a string. The potential can be approximated as harmonic and hence given by

$$V = \sum_{i=0}^N \frac{1}{2}m\omega_z^2 z_i^2 + \sum_{i \neq j}^N \frac{Z^2 e^2}{8\pi\epsilon_0} \frac{1}{|z_i - z_j|}, \quad (2.3.8)$$

where z_i is the position of the i -th ion, and Z the degree of ionization of the ions. The equilibrium positions can be found at the minima of the potential, i.e. where the first derivative zeros

$$\frac{\partial V}{\partial z_i} = 0 \implies u_i - \sum_{j=1}^{i-1} \frac{1}{(u_i - u_j)^2} + \sum_{j=i+1}^N \frac{1}{(u_i - u_j)^2} = 0, \quad (2.3.9)$$

where we defined the dimensionless quantity $u_i = z_i/l$ and $l^3 = \frac{Z^2 e^2}{4\pi\epsilon_0 m\omega^2}$. The last equation can be solved analytically for 2 or 3 ions [41]. For the case $N = 2$ we get the system

$$\begin{cases} u_1 + \frac{1}{(u_1 - u_2)^2} = 0 \\ u_2 - \frac{1}{(u_1 - u_2)^2} = 0 \end{cases} \implies u_1 = -u_2, \quad u_1 = \left(\frac{1}{2}\right)^{2/3} \simeq 0.629 \quad (2.3.10)$$

For $^{40}\text{Ca}^+$ ions (atomic mass $\simeq 40$ u [42]) in a Paul trap with axial confinement of $\omega_z = 2\pi \times 1$ MHz, we have $l \simeq 4.4 \times 10^{-6}$ m, which means that 2 ions are separated by $\simeq 5.6 \mu\text{m}$. This size is accessible since it is above diffraction limit (ref. section 2.4.1) for optical atomic transitions. In figure 2.3.2 ions positions are presented for different number of ions N trapped with an axial confinement of $\omega_z = 2\pi \times 1$ MHz.

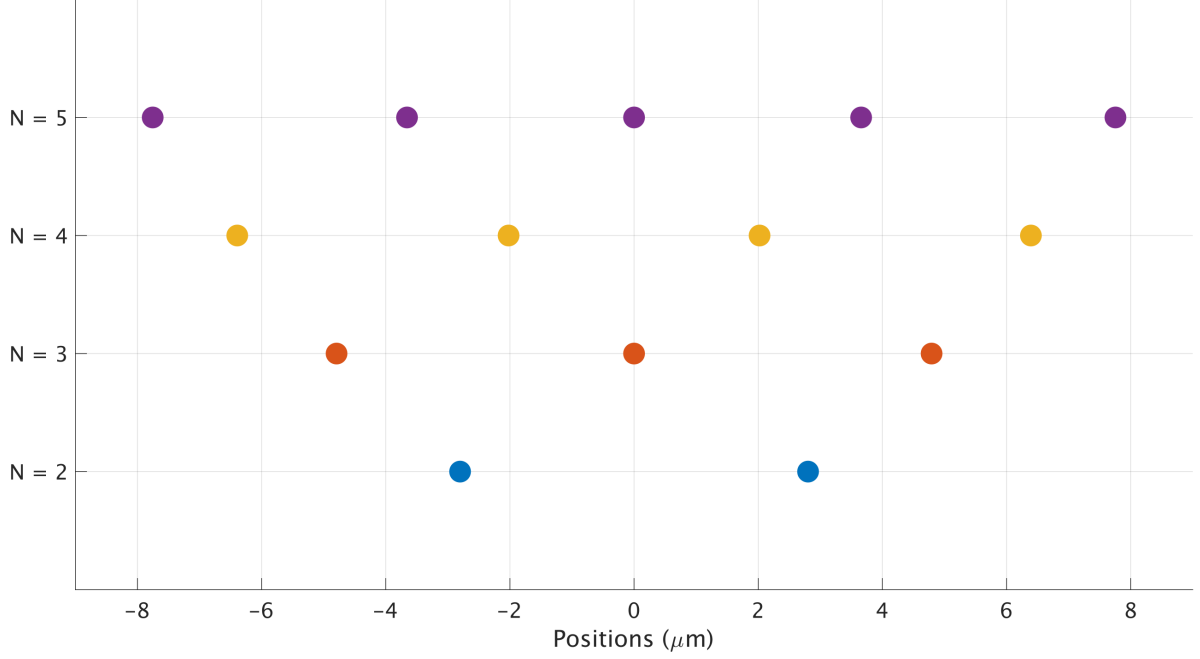


Figure 2.3.2: Ions position for different number N of ions in the trap. Confinement is $\omega_z = 2\pi \times 1$ MHz.

2.3.3 Doppler cooling

Coherent manipulation of ions requires cooling them to reach at least the Lamb Dicke regime [43], where the extent of the ion wave packet is much smaller than the optical wavelengths of the lasers. The idea comes from neutral atoms [44] and can be applied to ions as well: a laser interacts with a particular transition, exchanging a photon and therefore giving a momentum kick $\Delta p = \hbar \mathbf{k}$ in a particular direction to the ion. The absorbed photon is given back through spontaneous emission in a random direction, giving another kick to the ion. Over many cycles of absorption and emission, the random kick due to emission will average to zero, while the kick given by the laser will accumulate slowing down and cooling the ion in the direction of the laser.

The mathematical model is a 2-level atom interacting with a laser (Rabi frequency Ω , and detuning Δ) as described in section 2.1.2. Spontaneous emission is included with the master equation (2.1.25), where Γ is the spontaneous emission rate. The master equation can be explicitly written for every component of the density matrix ρ_{ij} , in the rotating frame they are called optical Bloch equations [45]. Following the approach of [46], the system reaches equilibrium when $\rho_{ee}(t \rightarrow \infty)$:

$$\rho_{ee}(t \rightarrow \infty) = \frac{\Omega^2/\Gamma^2}{1 + \left(2\frac{\Delta - \mathbf{k} \cdot \mathbf{v}}{\Gamma}\right)^2 + 2\frac{\Omega^2}{\Gamma^2}} \quad (2.3.11)$$

where \mathbf{v} the velocity of the ions. The force exerted on the ions, due to the radiative pressure, is proportional ρ_{ee} as

$$F = \hbar k \Gamma \rho_{ee} \simeq F_0 + \frac{dF}{dv} v = \hbar k \Gamma \frac{\Omega^2}{\Gamma^2 + 4\Delta^2} + F_0 \frac{8k\Delta}{\Gamma^2 + 4\Delta^2} v \quad (2.3.12)$$

where we assumed low velocities $v \simeq 0$ and thus linearized the equation. The effect of the constant term in the force is just to displace the ion from its central position. Instead, the linear term acts as a viscous friction that cools the ions with a rate of $\dot{E}_c = \langle Fv \rangle$. If on one side spontaneous emission allows for Doppler cooling, it also sets the lower limit. The small fluctuations in the Brownian motion leads to diffusion which heats the ion at a rate of

$$\dot{E}_h = \frac{1}{m} \frac{d}{dt} \langle p^2 \rangle = \frac{1}{m} (\hbar k)^2 \Gamma \langle \rho_{ee}(v) \rangle. \quad (2.3.13)$$

At equilibrium, the heating rate equals the cooling rate giving the lowest temperature achievable

$$\dot{E}_h + \dot{E}_c = 0 \implies k_B T = -\frac{\hbar \Gamma}{4} \left(\frac{\Gamma}{2\Delta} + \frac{2\Delta}{\Gamma} \right). \quad (2.3.14)$$

From here it is clear that by choosing the appropriated detuning, it is possible to reach the lowest temperature

$$T_{min} = \frac{\hbar \Gamma}{2k_B}, \quad \text{for } \Delta = -\frac{\Gamma}{2}. \quad (2.3.15)$$

At this temperature, the average phonon number is $\langle \hat{n} \rangle = \Gamma / 2\omega_z$ [47].

As an example, calcium ions confined in a trap with $\omega_z = 2\pi \times 1$ MHz, can be cooled using the transition $|S_{1/2}\rangle \rightarrow |P_{1/2}\rangle$ ($\Gamma = 2\pi \times 20.8$ MHz), the 2-level atom model in this case gives a good estimation, even though calcium has more levels. The Doppler temperature is $T_{min} \sim 500 \mu\text{K}$, and the corresponding average phonon number is $\langle \hat{n} \rangle = 10.4$. The wavefunction extend for this phonon number can be found as the standard deviation of the operator \hat{z} for the vibrational state $|n\rangle$, creation and annihilation operator algebra gives

$$\sigma_z = \sqrt{\langle \hat{z}^2 \rangle} = \sqrt{\frac{\hbar}{2m\omega_z} (1 + 2\langle \hat{n} \rangle)} \simeq 52 \text{ nm}. \quad (2.3.16)$$

An ion cooled with Doppler cooling therefore has a spatial dimension still much smaller than the ion separations.

To further decrease $\langle \hat{n} \rangle$, sideband cooling can be used [47], here particular sideband transitions are excited to reduce the phonon number of the ions inside the trap. However in the experiments of this thesis, only Doppler cooling has been performed.

2.4 Laser beam

2.4.1 Gaussian beams

Typically, lasers emit light in the shape of Gaussian beams, so it is import to understand what Gaussian beams are and their characteristics. In this chapter we will take a closer look into such beams and introduce important quantities to characterize a Gaussian beam. From a theoretical point of view, Gaussian beams are a particular solution of the Helmholtz equation $(\nabla^2 + k^2)U(\mathbf{r}) = 0$, with k being the wavevector, and $U(\mathbf{r})$ the complex electric field. If we can consider a wave propagating in the z direction, we can write it as [48]:

$$U(\mathbf{r}) = A_0 \frac{W_0}{W(z)} \exp \left\{ -\frac{x^2 + y^2}{W^2(z)} \right\} \exp \left\{ -ikz - ik \frac{x^2 + y^2}{2R(z)} + i \arctan(z/z_0) \right\}. \quad (2.4.1)$$

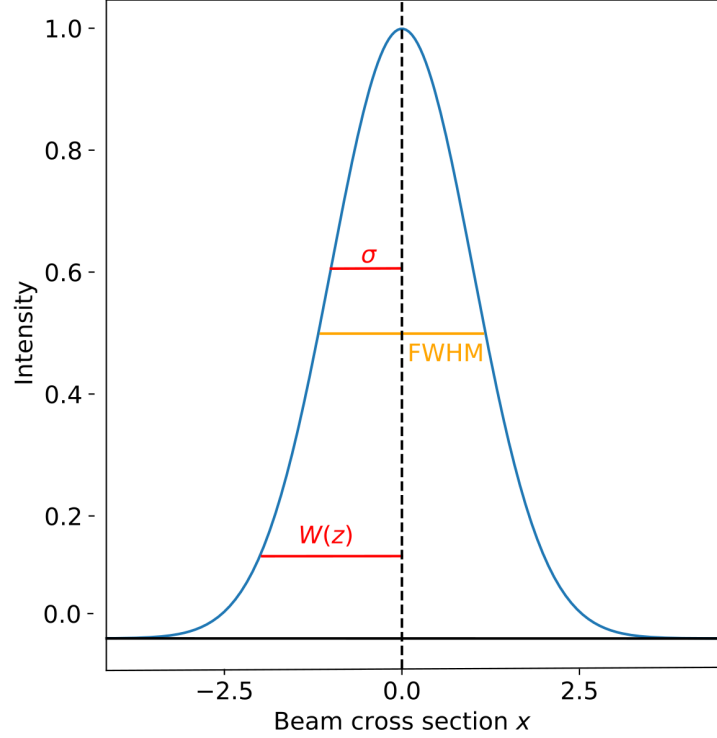


Figure 2.4.1: Cross section of the intensity profile of a Gaussian beam $I(x) = e^{-x^2/2\sigma^2}$. The beam is normalized and $\sigma = 1$. Graphical representations of used widths are displayed: $W(z)$ is defined as the point at which the intensity I has fallen to $1/e^2 = 13.5\%$ of its maximum value; σ is the standard deviation of a Gaussian in the form $Ae^{-\frac{x^2}{2\sigma^2}}$; FWHM is the full width half maximum. Relationships among these quantities are: $W(z) = 2\sigma$, and $W = 0.84 \cdot \text{FWHM}$.

Where A_0 is an amplitude, $W(z)$ the width, $R(z)$ the curvature radius, and z_0 the Rayleigh range. The intensity can be calculated by taking the square of the complex amplitude

$$I(\mathbf{r}) = |U(\mathbf{r})|^2 = I_0 \left(\frac{W_0}{W(z)} \right)^2 \exp \left\{ -\frac{2x^2 + 2y^2}{W^2(z)} \right\} \quad I_0 = |A_0|^2. \quad (2.4.2)$$

For a fixed z , i.e. the sections in the $x - y$ plane are shaped as a two dimensional Gaussian distribution. For simplicity, let us take the profile for a fixed z and $y = 0$:

$$I(x, y = 0, z) = \tilde{A}(z) \exp \left\{ \frac{2x^2}{W^2(z)} \right\} \quad \tilde{A}(z) = I_0 \left(\frac{W_0}{W(z)} \right)^2. \quad (2.4.3)$$

In Figure 2.4.1, the x cross section is depicted for this intensity profile normalized in amplitude. Parameters used to measure the width are also displayed and defined in the caption. All of those quantities are equivalent and differ only by a prefactor, so for the rest of the section, we stick to $W(z)$ and study its behaviour. From Helmholtz equation [48], the profile of $W(z)$ as a function of z is found to be

$$W(z) = W_0 \sqrt{1 + \left(\frac{z}{z_0} \right)^2} \quad W_0 = \sqrt{\frac{\lambda z_0}{\pi}} \quad z_0 = \frac{\pi W_0^2}{\lambda}. \quad (2.4.4)$$

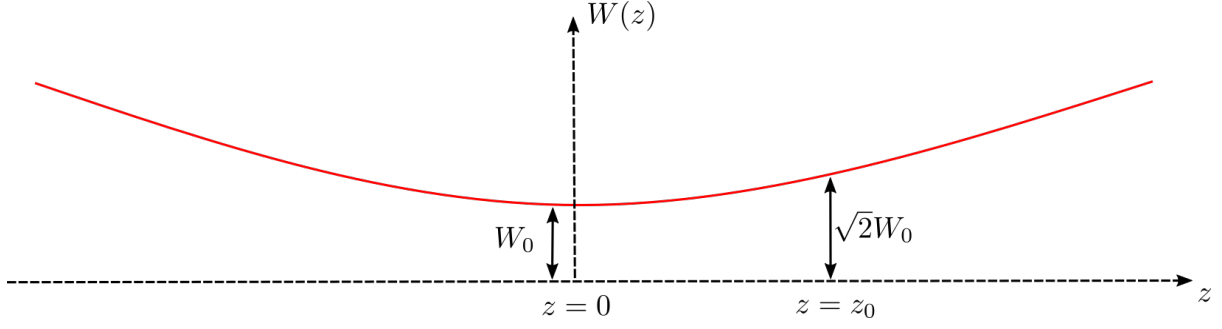


Figure 2.4.2: Width profile of a Gaussian beam along the direction of travel of the beam, equation (2.4.4). The beam is focused at the position $z = 0$, here it assumes the minimum width W_0 , also referred to as the waist. z_0 is the Rayleigh range where the width is $\sqrt{2}W_0$

λ is the wavelength, and W_0 and z_0 are respectively the waist of the beam and the Rayleigh range discussed below. A plot of (2.4.4) is presented in Figure (2.4.2): the width $W(z)$ assumes its minimum value W_0 at $z = 0$, this spot is called focus and its width W_0 is the waist of the beam. The Rayleigh range z_0 gives an idea of how quickly the beam is expanding. Mathematically z_0 is the distance between the focus and the point where the width $W(z)$ is exactly $\sqrt{2}W_0$. For $z \gg z_0$, the beam profile diverges almost linearly with an angle given by $\theta = W_0/z_0$, which means the smaller the focus, the greater it diverges. This property will become important later in the work, because it provides one limit on the waist of the beam in our experimental system. In fact, the optical aperture of the trap is limited by some electrodes, and a beam that diverges too rapidly can potentially clip on one electrode causing aberrations and scattered light in the trap.

A Gaussian beam can be reshaped using optical elements. In order to study such reshaping, let us consider a thin spherical lens with focal length f , and radius of curvature R_l placed at position z . The effect of the lens on the beam is to give an extra phase factor $k(x^2 + y^2)/2f$ to equation (2.4.1) [49]. We can match the phase of the incoming and emerging waves, which have respectively radius of curvature R , and R' , this results in

$$\frac{1}{R'} = \frac{1}{R} - \frac{1}{f}. \quad (2.4.5)$$

The effect of the lens is to change the radius of curvature to R' . Moreover, the width of the beam at the lens is not altered $W = W'$. Using these last two facts, we can determine all the parameters of the outgoing wave. The most important for us is the new waist W'_0

$$W'_0 = MW_0 \quad M = \frac{M_r}{\sqrt{q + r^2}} \quad M_r = \left| \frac{f}{z - f} \right| \quad r = \frac{z_0}{z - f}. \quad (2.4.6)$$

M is the magnification factor which provides an easy way to describe the change of the beam. For a better understanding of this last result, let us consider an less general example. We place the lens at the focus $z = 0$, and have a collimated beam $z_0 \rightarrow +\infty$. In this case the new waist is

$$W'_0 = \frac{W_0}{\sqrt{1 + (z_0/f)^2}} \simeq W_0 \frac{f}{z_0} = \frac{\lambda f}{\pi W_0} \quad (2.4.7)$$

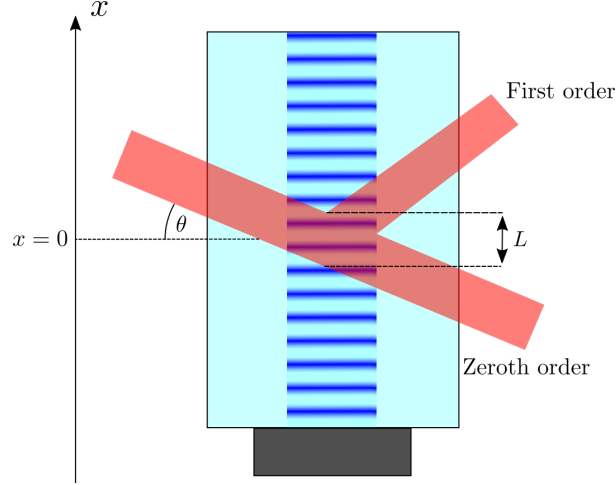


Figure 2.4.3: Simple model of an AOD. In black at the bottom a black piezo that generates acoustic waves through the light blue crystal. In red, a collimated beam of light enters in the crystal with an angle θ and gets partially deflected due to the interaction with the effective optical grating created by the acoustic waves.

where the approximation comes from taking $z_0 \gg f$. There are three parameters we can act on to achieve the smallest focus spot: (a) the wavelength λ , the shorter the better; (b) the focal length of the lens f , smaller focus with shorter focal length; (c) the waist of the incoming beam W_0 , larger waist corresponds to narrower focus.

An optical system performing to the theoretical limit is said to be diffraction limited. In the instance of a focusing system, it corresponds to the case where the collimated beam diameter $2W_0$ is equal to the diameter D of the focusing lens. Equation 2.4.7 becomes

$$W_0 = \frac{2\lambda}{\pi} \frac{f}{D}. \quad (2.4.8)$$

If the size of the collimated beam is further increased, the lens becomes a finite size aperture and diffraction effects will appear at the image plane.

2.4.2 Beam steering via Acousto-optical Deflectors

An acousto-optical deflector (AOD) is a common device that can change the propagation direction of a laser beam, typically on the few microsecond timescale. In this work we use an AOD to change which ion is illuminated by a single-ion focused laser. The working principle of an AOD is based on the Acousto-optical effect. A piezo is used to create acoustic waves that propagate through a crystal. The waves modify the crystal refractive index, creating a periodic optical grating that can deflect light travelling through it.

Following the approach of [48] to model the device, let us consider a rectangular crystal like in figure 2.4.3. The acoustic wave creates a sinusoidal pattern with frequency Ω_s and wavevector q , for the refractive index $n(x, t)$

$$n(x, t) = n - \Delta n_0 \cos(\Omega_s t - qx), \quad (2.4.9)$$

where n is the refractive index of the unperturbed medium, Δn_0 is the amplitude of the perturbation. Δn_0 is proportional to the square root of the sound intensity. The complex

amplitude of the refracted wave r can be calculated by dividing the crystal in thin layers, each with his refractive index $n(x)$. The total refraction is given by all the contributions $\frac{dr}{dx}$ of every layer, we can therefore integrate in the x direction over the length L as follow:

$$r = \int_{L/2}^{L/2} e^{i2kx \sin \theta} \frac{dr}{dx} dx \quad (2.4.10)$$

The included phase takes into consideration the different phase of the input beam when different layers are met. The integral can be solved with a change of variable

$$\frac{dr}{dx} = \frac{dr}{dn} \frac{dn}{dx} = \frac{dr}{dn} q \Delta n_0 \sin(\Omega_s t - qx), \quad (2.4.11)$$

The sine function can be written as exponential and now the integral contains only exponential functions which are trivial to calculate. At the end we obtain two contributions for the refracted wave r :

$$r = r_+ + r_- \quad r_{\pm} = \pm i r_0 \text{sinc} \left[(2k \sin \theta \mp q) \frac{L}{2\pi} \right] e^{\pm i \Omega_s t} \quad (2.4.12)$$

These two terms are the plus and minus first order diffraction, an acousto-optical device can be operated symmetrically entering either with a positive angle or with a negative one. Since the maths and the physics is the same, we will focus only on the positive term, called upshifted Bragg diffraction. The sinc function peaks sharply when its argument is 0, i.e. at $2k \sin \theta = q$, and then quickly decreases as the angle is changed. Hence, the input beam must enter with a particular angle in order to diffract with maximum efficiency. The condition to be satisfied is called Bragg condition, and can be written as a function of the optical λ and acoustic Λ_s wavelengths as

$$\sin \theta = \frac{\lambda}{2\Lambda_s} \quad \Lambda_s = \frac{2\pi}{q}. \quad (2.4.13)$$

If the condition is not perfectly matched, some light will not be diffracted and will be transmitted unaltered through the device. The ratio of the transmitted and diffracted light is called diffraction efficiency and gives an idea of how well an acousto-optical device is performing.

From equation (2.4.12) we can notice that an extra phase factor proportional to $\Omega_s t$ is added to the reflected wave. Thus, if the incoming wave is oscillating at $\propto e^{i\omega t}$, the diffracted wave will oscillate as $\propto r_+ e^{i\omega t} \implies \propto e^{i(\omega + \Omega_s)t}$. The frequency of the diffracted wave ω_r is therefore shifted by the frequency of the acoustic vibration as

$$\omega_r = \omega + \Omega_s. \quad (2.4.14)$$

The acousto-optical effect described above is common to different devices optimized for specific tasks. Two of the most commons devices are Acousto-optical Deflectors (AOD) and Acousto-optical Modulators (AOM). The idea of the latter is to shift the frequency of a laser using equation (2.4.14). Deflectors instead exploit the fact that the deflection angle θ changes linearly as a function of the acoustic frequency Ω_s . Assuming that the

angle θ is small enough to approximate $\sin \theta \sim \theta$, the Bragg condition can be written as

$$\theta \simeq \frac{\lambda}{2v_s} f, \quad (2.4.15)$$

where v_s is the speed of sound and f the frequency of the acoustic wave. We can already see that if we change the frequency f , the deflection angle θ changes proportionally. Although the Bragg condition (2.4.13) is not satisfied anymore, we can work with small enough angles that the diffraction efficiency remains above a certain threshold. The bandwidth B specifies the range of frequencies over which deflectors work.

AOMs and AODs differ by the relative divergence of the optical and acoustic beam [50], moreover for AODs, speed and the number of resolvable spots are more important, while for AOM's the optimization is on modulation bandwidth. These different priorities in building the devices influence the choice of the crystal and acoustic mode, for instance, a slow acoustic velocity and shear mode are preferred in AODs [50]. More advanced techniques to engineer an AOD are available, for example the piezo is replaced by a phase array of transducers that tilt the acoustic beam [51].

As already stated, in the experiment setup of this work, an AOD is used to steer a single-ion focused laser and aim at different ions in the μs timescale. AOMs instead are extensively used to tune and scan the laser frequencies.

2.5 Experiments model

The aim of this thesis is to perform two experiments with ions: qubit manipulation, and photon generation. In addition to test these two functionalities, the experiments are also designed to assess the performance of the addressing system as discussed below. In both cases a string of 3-4 ions is loaded in the trap, the addressed Raman laser is focused on a single ion and experiments are carried out.

2.5.1 Addressed qubit manipulation

As we have seen, ions can be used to encode and process quantum information. As highlighted in figure 2.5.1, the qubit is encoded in the $|S\rangle \rightarrow |D\rangle$ transition. The 393nm transition from $|S\rangle \rightarrow |P\rangle$ can be used to induce a phase shift on the ground state of the qubit $|S\rangle$. In the off resonant regime, the laser induces a Stark shift $\delta = \Omega^2/4\Delta$ without actually exciting the state. As discussed in section 2.1.2.2, in order for this to happen, we should have $\delta \gg \Gamma_{eff}$. Therefore in the experiment we decided to set the detuning such that the ratio between the Stark shift and the spontaneous scattering rate is 100

$$\frac{\delta}{\Gamma_{eff}} = \frac{2\Delta}{\Gamma} \sim 100 \implies \Delta \sim 3 \text{ GHz}. \quad (2.5.1)$$

Furthermore, ions can be used as sensitive tools for beam profiling, the addressed manipulation changes only the qubit state of a single ion. Hence, by measuring the state of all ions, and scanning the beam across the ions string, a beam profile can be obtained. In a single experiment we can therefore characterize the beam and demonstrate qubit manipulation. The experiment consists of Ramsey interferometry, already performed in the past to measure AC Stark shift [16]. In summary, the idea is to send a resonant $\pi/2$

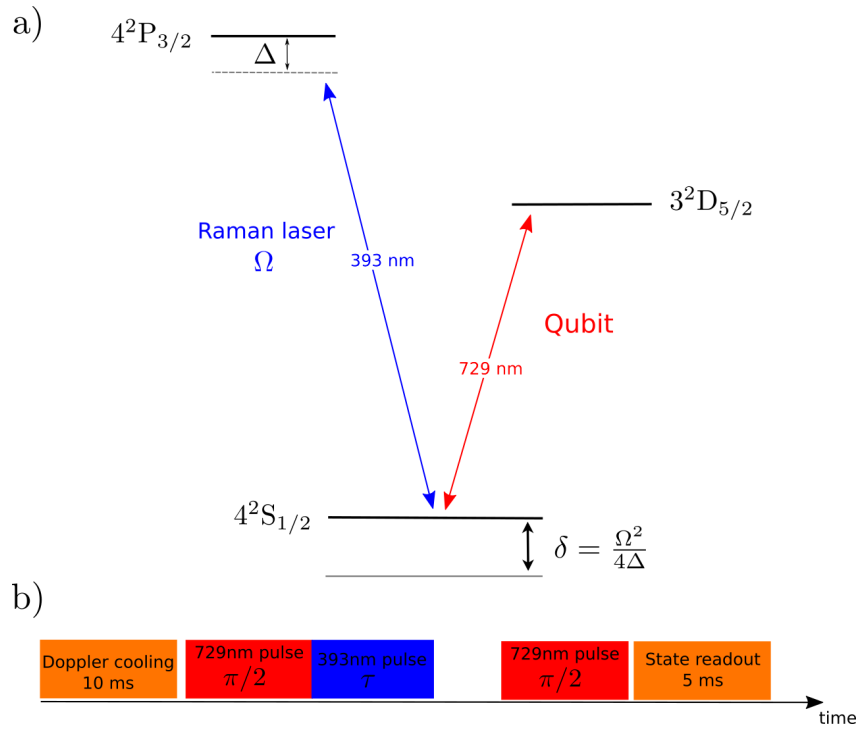


Figure 2.5.1: a) Relevant levels for the experiment, the qubit is encoded in the 729 nm transition, the 393 nm laser is used to shift the $|S\rangle$ level via AC Stark shift b) Experiment pulse sequence, Doppler cooling and state readout are described in section ???. The time τ had a variable length.

pulse at 729 nm, which brings the qubit state to a superposition $|S\rangle + |D\rangle$, here another in phase resonant $\pi/2$ pulse at 729 nm would bring the final state to the excited level $|D\rangle$. However, if between the two 729 nm pulses, AC stark shift is induced by a pulse of 393 nm light, an additional phase is added to the superposition $|S\rangle + |D\rangle$, and the final state after the second 729 nm pulse will depend on the shift induced by the 393nm laser. The phase of the second 729 nm pulse can also be varied. By calculating the final probability P_D it is possible to infer the Rabi frequency of the 393 nm light. Rigorous mathematic can be done with matrices (2.1.15) here called U_{729} and (2.1.20), referred to as U_{393} . After the three pulse sequence the final state is

$$\begin{aligned} |\psi_f\rangle &= U_{729}(\pi, \phi) U_{393}(\delta) U_{729}(\pi, 0) |S\rangle \\ &= \frac{1}{2} \left(e^{-i\frac{\delta}{2}\tau} - e^{-i\phi} \right) |S\rangle - \frac{i}{2} \left(1 + e^{-i\frac{\delta}{2}\tau} e^{-i\phi} \right) |D\rangle \end{aligned} \quad (2.5.2)$$

where $\delta = \Omega^2/4\Delta$ is the Stark shift, and Ω is the Rabi frequency of the 393nm light that we want to measure. The final probability is then

$$P_D = \cos^2 \left(2\phi + 2\frac{\delta\tau}{2} \right) = \cos^2 \left(2\phi + \frac{\Omega^2\tau}{4\Delta} \right). \quad (2.5.3)$$

As we can see, the final signal depends on the phase of the second 729nm pulse ϕ and on the Stark shift induced by the 393nm laser. To get Ω^2 a simple formula inversion can be done

$$\Omega^2 = \left[\arccos \left(\sqrt{P_D} \right) - 2\phi \right]. \quad (2.5.4)$$

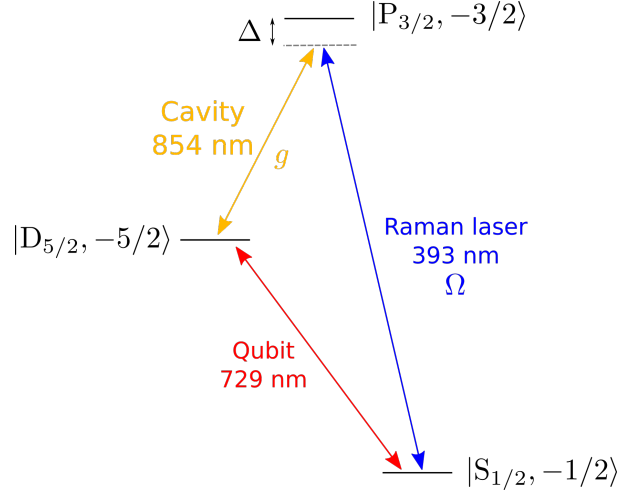


Figure 2.5.2: Scheme of the Raman process used to generate photons, via a cavity enhanced Raman process (Section 2.2.3). The electron in the $|S\rangle$ state is excited to the $|D\rangle$ level by absorbing a 393 nm photon and emitting a 854 nm photon in the cavity.

The phase ϕ can be set experimentally and all constants have been dropped as the data will be normalized. The experiment sequence is in figure 2.5.1. For every sequence, a stage of Doppler Cooling at the beginning is included and at the end of the pulses state readout with single-ion resolving camera is performed. For each 393 nm pulse length τ the sequence is repeated $N = 50$ times to obtain and estimate the electronic excitation probability.

2.5.2 Addressed photon generation

The second experiment consists of generating photons from one single ion, using the Raman process described in section 2.2.3. In figure 2.5.2 the relevant levels are depicted. In this case the ion is positioned in a maximum of the cavity electric field such that the coupling atom-cavity g is maximized. A 393 nm laser pulse triggers the generation of a photon in the cavity through a Raman process as described in section 2.2.3. The detunings of the cavity and laser pulse must be equal, moreover the detuning should be large enough to adiabatically eliminate the P state and avoid spontaneous scattering. As seen in section 2.2.3, this is ensured by a detuning of $\Delta \sim 400$ MHz. In this process the population of the state $|S\rangle$ is coherently transferred to the $|D\rangle$ state by absorbing a 393 nm photon and emitting a 854 nm photon in the cavity, the photon then exits from the cavity. The states involved in the dynamics are

$$|S_{1/2}, -1/2\rangle \rightarrow |P_{3/2}, -3/2\rangle \rightarrow |D_{5/2}, -5/2\rangle. \quad (2.5.5)$$

Note that the effective Rabi frequency of the population transfer is proportional to the laser drive Rabi frequency $\propto \Omega$ as seen in equation (2.2.7). On the contrary, AC Stark shift depends on the Intensity $\propto \Omega^2$. Therefore, the addressing error in the two experiments are different. After the excitation and photo emission, state detection on all ions is performed, this gives the possibility to check if other ions have been unwantedly addressed.

Chapter 3

Conclusions and outlook

In this thesis works, an optical setup for single ion focusing of 393 nm laser has been designed and built. The design was based on the already successful addressing setups built in other experiments, but it has been improved to avoid clipping that limited the addressing range. The software Zemax was used to simulate, and check the performance of the design. Optimal lenses for the construction were also found with the software. Once the simulation was satisfactory, a test setup was built on an optical table where it has been characterized in terms of performance, polarization capabilities, and stability. Here the smallest waist measured was $2.4\ \mu\text{m}$, the switching time of the AOD was in the order of $7\text{-}8\ \mu\text{s}$, and addressing range $>150\ \mu\text{m}$. Afterwards, the setup was moved and aligned on the ions, where limited physical access did not allow for such easy checks, but instead more advanced quantum optics experiments have been performed.

The setup was intended to be used for single photon generations and single qubit manipulations. Both of the purposes has been fulfilled: the photon generation was demonstrated in the experiment in section ??, here a string of three ions was loaded into the trap and the focused laser aligned with the central one. A laser pulse triggered the photon generation exclusively from the intended ion. The photon detection probability was $< 15\%$, and can definitely be further improved as particular attention was not given to the polarization, but the system already has the capabilities for precise polarization setting. Permanent magnets are still mounted parallel to the previous Raman laser direction, they can be moved in the new direction to improve photon emission. Qubit manipulation was carried out in the Ramsey interferometer experiment, here we measured the AC stark shift caused by the 393 nm light by imprinting a phase on the qubit encoded in the 729 nm transition. State readout of the qubits showed the different final states for different phases due to the 393 nm light. Moreover, with this experiment the waist of beam was measured to be $1.2 - 1.3\ \mu\text{m}$ and the addressing error was estimated to have an upper bound of 10^{-3} .

The next natural step is the generation of photons from different ions currently undergoing at the moment of this thesis writing. Afterwards, entanglement can also be produced between a single ion and a photon, once more stabilization improvement on the setup are done. This project has several future development, on the quantum network side, this work represents an improved interface between network and quantum computer, transmission bandwidth has drastically increased, dedicated qubits for networking, storing, and computation can now be created and manipulated. It also opens up to the possibility to create multi-ion-multi-photon states with applications in quantum metrology.

Bibliography

- [1] Antonio Acín, Immanuel Bloch, Harry Buhrman, Tommaso Calarco, Christopher Eichler, Jens Eisert, Daniel Esteve, Nicolas Gisin, Steffen J Glaser, Fedor Jelezko, Stefan Kuhr, Maciej Lewenstein, Max F Riedel, Piet O Schmidt, Rob Thew, Andreas Wallraff, Ian Walmsley, and Frank K Wilhelm. The quantum technologies roadmap: a european community view. *New Journal of Physics*, 20(8):080201, aug 2018.
- [2] Peter W. Shor. Polynomial-time algorithms for prime factorization and discrete logarithms on a quantum computer. *SIAM J. Comput.*, 26(5):1484–1509, oct 1997.
- [3] Lov K. Grover. A fast quantum mechanical algorithm for database search. In *Proceedings of the Twenty-eighth Annual ACM Symposium on Theory of Computing*, STOC '96, pages 212–219, New York, NY, USA, 1996. ACM.
- [4] I. M. Georgescu, S. Ashhab, and Franco Nori. Quantum simulation. *Rev. Mod. Phys.*, 86:153–185, Mar 2014.
- [5] H. J. Kimble. The quantum internet. *Nature*, 453(7198):1023–1030, jun 2008.
- [6] Stephanie Wehner, David Elkouss, and Ronald Hanson. Quantum internet: A vision for the road ahead. *Science*, 362(6412), 2018.
- [7] *Proceedings of IEEE International Conference on Computers, Systems and Signal Processing*, 1984.
- [8] Ivan B. Damgård, Serge Fehr, Louis Salvail, and Christian Schaffner. Cryptography in the bounded quantum-storage model. In *Proceedings of the 46th Annual IEEE Symposium on Foundations of Computer Science*, FOCS '05, pages 449–458, Washington, DC, USA, 2005. IEEE Computer Society.
- [9] Joseph F. Fitzsimons. Private quantum computation: an introduction to blind quantum computing and related protocols. *npj Quantum Information*, 3(1), jun 2017.
- [10] P. Kómár, E. M. Kessler, M. Bishof, L. Jiang, A. S. Sørensen, J. Ye, and M. D. Lukin. A quantum network of clocks. *Nature Physics*, 10(8):582–587, jun 2014.
- [11] Daniel Gottesman, Thomas Jennewein, and Sarah Croke. Longer-baseline telescopes using quantum repeaters. *Phys. Rev. Lett.*, 109:070503, Aug 2012.
- [12] Vasil S. Denchev and Gopal Pandurangan. Distributed quantum computing: A new frontier in distributed systems or science fiction? *SIGACT News*, 39(3):77–95, September 2008.
- [13] J. I. Cirac and P. Zoller. Quantum computations with cold trapped ions. *Phys. Rev. Lett.*, 74:4091–4094, May 1995.

- [14] Andreas Stute, Bernardo Casabone, Bernhard Brandstätter, Dr. M. Habicher, H. G. Barros, Piet O. Schmidt, Tracy E. Northup, and Rainer Blatt. Toward an ion–photon quantum interface in an optical cavity. *Applied Physics B*, 107:1145–1157, 2012.
- [15] Isaac L. Chuang Michael A. Nielsen. *Quantum computation and quantum information*. Cambridge Series on Information and the Natural Sciences. Cambridge University Press, 1 edition, 2004.
- [16] H. Häffner, S. Gulde, M. Riebe, G. Lancaster, C. Becher, J. Eschner, F. Schmidt-Kaler, and R. Blatt. Precision measurement and compensation of optical stark shifts for an ion-trap quantum processor. *Phys. Rev. Lett.*, 90:143602, Apr 2003.
- [17] Cornelius Hempel. *Digital quantum simulation, Schroedinger cat state spectroscopy and setting up a linear ion trap*. PhD thesis, University of Innsbruck, 2014.
- [18] Christian Roos. *Controlling the quantum state of trapped ions*. PhD thesis, University of Innsbruck, 2000.
- [19] Daniel Adam Steck. Quantum and atom optics.
- [20] D.F.V. James. Quantum computation with hot and cold ions: An assessment of proposed schemes. *Fortschritte der Physik*, 48(9-11):823–837, 2000.
- [21] Carlos Manuel da Silva Baptista Russo. *Photon statistics of a single ion coupled to a high-finesse cavity*. PhD thesis, University of Innsbruck, 2008.
- [22] P. Zoller C. Gardiner. *Quantum Noise*. Springer-Verlag Berlin Heidelberg, 2004.
- [23] Richard J Hughes, Jane E Nordholt, Derek Derkacs, and Charles G Peterson. Practical free-space quantum key distribution over 10 km in daylight and at night. *New Journal of Physics*, 4:43–43, July 2002.
- [24] L.-M. Duan and C. Monroe. Colloquium: Quantum networks with trapped ions. *Rev. Mod. Phys.*, 82:1209–1224, Apr 2010.
- [25] Stephan Ritter, Christian Nölleke, Carolin Hahn, Andreas Reiserer, Andreas Neuzner, Manuel Uphoff, Martin Mücke, Eden Figueroa, Joerg Bochmann, and Gerhard Rempe. An elementary quantum network of single atoms in optical cavities. *Nature*, 484(7393):195–200, apr 2012.
- [26] W. K. Wootters and W. H. Zurek. A single quantum cannot be cloned. *Nature*, 299(5886):802–803, oct 1982.
- [27] H.-J. Briegel, W. Dür, J. I. Cirac, and P. Zoller. Quantum repeaters: The role of imperfect local operations in quantum communication. *Phys. Rev. Lett.*, 81:5932–5935, Dec 1998.
- [28] Jian-Wei Pan, Christoph Simon, Ľaslav Brukner, and Anton Zeilinger. Entanglement purification for quantum communication. *Nature*, 410(6832):1067–1070, April 2001.
- [29] Charles H. Bennett, Gilles Brassard, Claude Crépeau, Richard Jozsa, Asher Peres, and William K. Wootters. Teleporting an unknown quantum state via dual classical and einstein-podolsky-rosen channels. *Phys. Rev. Lett.*, 70:1895–1899, Mar 1993.

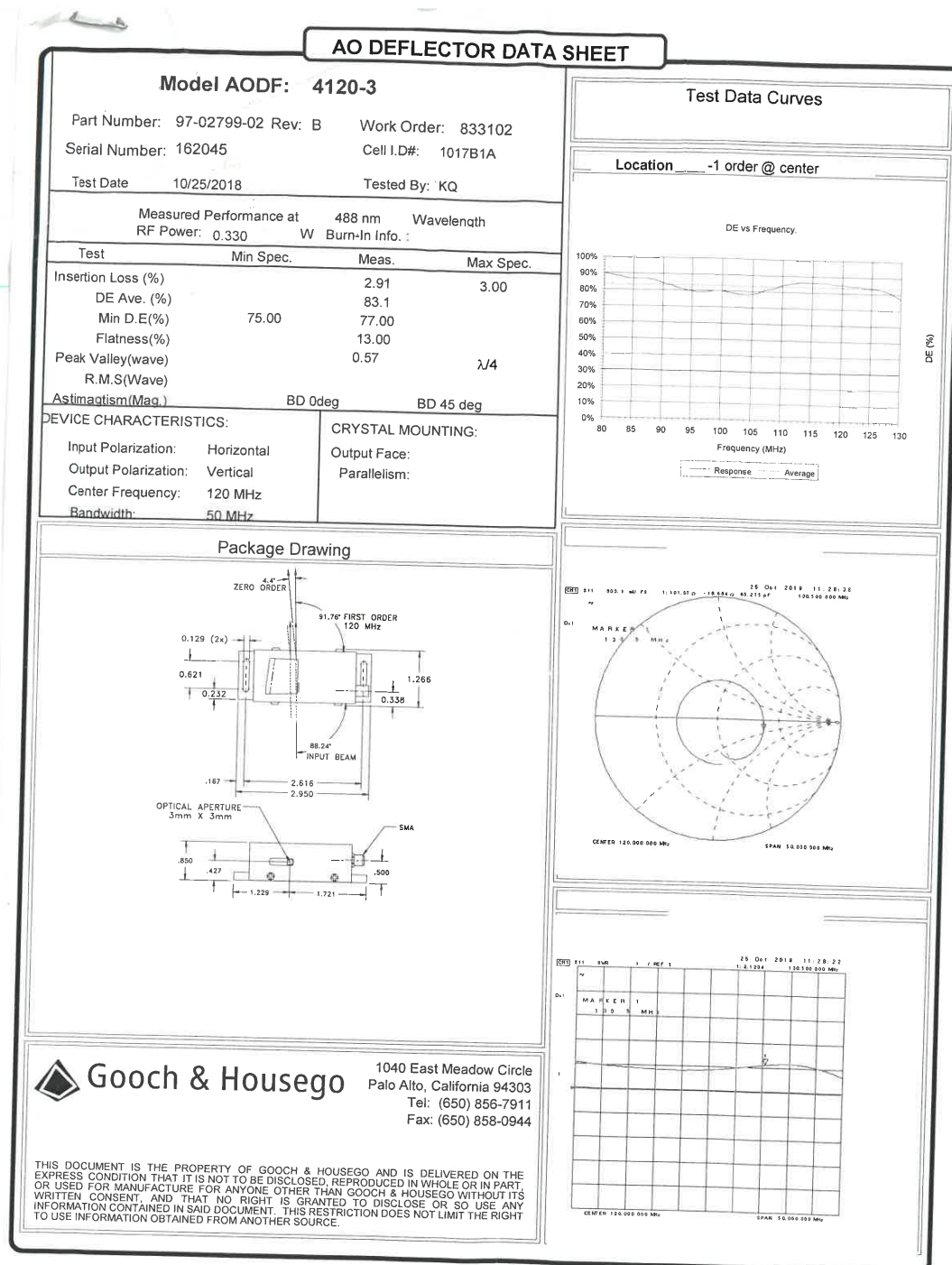
- [30] G. Araneda, D. B. Higginbottom, L. Slodička, Y. Colombe, and R. Blatt. Interference of single photons emitted by entangled atoms in free space. *Phys. Rev. Lett.*, 120:193603, May 2018.
- [31] Matthias Keller, Birgit Lange, Kazuhiro Hayasaka, Wolfgang Lange, and Herbert Walther. Continuous generation of single photons with controlled waveform in an ion-trap cavity system. *Nature*, 431(7012):1075–1078, October 2004.
- [32] H. J. Kimble. Strong interactions of single atoms and photons in cavity QED. *Physica Scripta*, T76(1):127, 1998.
- [33] Helmut Ritsch, Peter Domokos, Ferdinand Brennecke, and Tilman Esslinger. Cold atoms in cavity-generated dynamical optical potentials. *Rev. Mod. Phys.*, 85:553–601, Apr 2013.
- [34] Helene Hainzer. Laser locking for trapped-ion quantum networks. Master’s thesis, University of Innsbruck, 2018.
- [35] H. G. Barros, A. Stute, T. E. Northup, C. Russo, P. O. Schmidt, and R. Blatt. Deterministic single-photon source from a single ion. *New Journal of Physics*, 11(10):103004, October 2009.
- [36] V. Krutyanskiy, M. Meraner, J. Schupp, V. Krcmarsky, H. Hainzer, and B. P. Lanyon. Light-matter entanglement over 50 km of optical fibre. *npj Quantum Information*, 5(1), August 2019.
- [37] Lowell S. Brown and Gerald Gabrielse. Geonium theory: Physics of a single electron or ion in a penning trap. *Rev. Mod. Phys.*, 58:233–311, Jan 1986.
- [38] Philip E. Miller and M. Bonner Denton. The quadrupole mass filter: Basic operating concepts. *Journal of Chemical Education*, 63(7):617, 1986.
- [39] J. A. Richards. *The Mathieu Equation*, pages 93–107. Springer Berlin Heidelberg, Berlin, Heidelberg, 1983.
- [40] D. Leibfried, R. Blatt, C. Monroe, and D. Wineland. Quantum dynamics of single trapped ions. *Rev. Mod. Phys.*, 75:281–324, Mar 2003.
- [41] D. F. V. James. Quantum dynamics of cold trapped ions with application to quantum computation. *Applied Physics B: Lasers and Optics*, 66(2):pp. 181–90.
- [42] G. Audi, A.H. Wapstra, and C. Thibault. The ame2003 atomic mass evaluation: (ii). tables, graphs and references. *Nuclear Physics A*, 729(1):337 – 676, 2003. The 2003 NUBASE and Atomic Mass Evaluations.
- [43] D.J. Wineland, C. Monroe, W.M. Itano, D. Leibfried, B.E. King, and D.M. Meekhof. Experimental issues in coherent quantum-state manipulation of trapped atomic ions. *Journal of Research of the National Institute of Standards and Technology*, 103(3):259, May 1998.
- [44] T. W. Hansch and A. L. Schawlow. Cooling of gases by laser radiation. *Optics Communications*, 13(1):68–69, Jan 1975.
- [45] C.J. Foot. *Atomic Physics*. Oxford Master Series in Physics, 2004.

- [46] Gabriel Andres Areneda Machuca. *Experiments with single photons emitted by single atoms*. PhD thesis, University of Innsbruck, 2019.
- [47] Jürgen Eschner, Giovanna Morigi, Ferdinand Schmidt-Kaler, and Rainer Blatt. Laser cooling of trapped ions. *J. Opt. Soc. Am. B*, 20(5):1003–1015, May 2003.
- [48] Bahaa E. A. Saleh and Malvin Carl Teich. *Fundamentals of photonics*. Wiley Series in Pure and Applied Optics, 2 edition, 2007.
- [49] C. S. Williams. Gaussian beam formulas from diffraction theory. *Appl. Opt.*, 12(4):872–876, Apr 1973.
- [50] Michael Bass, Eric W. Van Stryland, David R. Williams, and Williams L. Wolfe. *Handbook of Optics Volume II Devices, Measurements, and Properties 2nd edition*. 1995.
- [51] R. Pieper, D. Koslover, and H. Ndawata. Combining phased array and hamming sound apodization techniques to improve the acousto-optic diffraction bandwidth. In *2009 41st Southeastern Symposium on System Theory*, pages 311–316, March 2009.
- [52] H. Ball, M. W. Lee, S. D. Gensemer, and M. J. Biercuk. A high-power 626 nm diode laser system for beryllium ion trapping. *Review of Scientific Instruments*, 84(6):063107, 2013.
- [53] M. R. Dietrich, N. Kurz, T. Noel, G. Shu, and B. B. Blinov. Hyperfine and optical barium ion qubits. *Phys. Rev. A*, 81:052328, May 2010.
- [54] D. J. Berkeland. Linear paul trap for strontium ions. *Review of Scientific Instruments*, 73(8):2856–2860, 2002.
- [55] H. C. Nägerl, Ch. Roos, D. Leibfried, H. Rohde, G. Thalhammer, J. Eschner, F. Schmidt-Kaler, and R. Blatt. Investigating a qubit candidate: Spectroscopy on the $S_{1/2}$ to $D_{5/2}$ transition of a trapped calcium ion in a linear paul trap. *Phys. Rev. A*, 61:023405, Jan 2000.
- [56] A. S. Bell, P. Gill, H. A. Klein, A. P. Levick, Chr. Tamm, and D. Schnier. Laser cooling of trapped ytterbium ions using a four-level optical-excitation scheme. *Phys. Rev. A*, 44:R20–R23, Jul 1991.
- [57] R.C. Thompson, G.P. Barwood, and P. Gill. Laser cooling of magnesium ions confined in a penning trap. *Optica Acta: International Journal of Optics*, 33(4):535–543, 1986.
- [58] R. Blatt, H. Häffner, C. F. Roos, C. Becher, and F. Schmidt-Kaler. Ion trap quantum computing with Ca^+ ions. *Quantum Information Processing*, 3(1-5):61–73, October 2004.
- [59] T. Ruster, C. T. Schmiegelow, H. Kaufmann, C. Warschburger, F. Schmidt-Kaler, and U. G. Poschinger. A long-lived zeeman trapped-ion qubit. *Applied Physics B*, 122(10), September 2016.
- [60] Andreas tute. *A light-matter quantum interface: ion-photon entanglement and state mapping*. PhD thesis, University of Innsbruck, 2012.

- [61] S. Gulde, D. Rotter, P. Barton, F. Schmidt-Kaler, R. Blatt, and W. Hogervorst. Simple and efficient photo-ionization loading of ions for precision ion-trapping experiments. *Applied Physics B*, 73(8):861–863, December 2001.
- [62] H. C. Nägerl, D. Leibfried, H. Rohde, G. Thalhammer, J. Eschner, F. Schmidt-Kaler, and R. Blatt. Laser addressing of individual ions in a linear ion trap. *Phys. Rev. A*, 60:145–148, Jul 1999.
- [63] S. Crain, E. Mount, S. Baek, and J. Kim. Individual addressing of trapped 171yb^+ ion qubits using a microelectromechanical systems-based beam steering system. *Applied Physics Letters*, 105(18):181115, 2014.
- [64] M. Johanning, A. Braun, N. Timoney, V. Elman, W. Neuhauser, and Chr. Wunderlich. Individual addressing of trapped ions and coupling of motional and spin states using rf radiation. *Phys. Rev. Lett.*, 102:073004, Feb 2009.
- [65] Fiber Collimators 60FC. <https://www.sukhamburg.com/download/fibercollimators60fc.pdf>.
- [66] M. Riedl. *Optical Design Fundamentals for Infrared Systems*. SPIE Press, 2011.
- [67] Yasuzi Suzuki and Atsushi Tachibana. Measurement of the μm sized radius of gaussian laser beam using the scanning knife-edge. *Applied Optics*, 14(12):2809, December 1975.
- [68] Bruce Cannon, Timothy S. Gardner, and Donald K. Cohen. Measurement of $1\text{-}\mu\text{m}$ diam beams. *Appl. Opt.*, 25(17):2981–2983, Sep 1986.
- [69] William H. McMaster. Polarization and the stokes parameters. *American Journal of Physics*, 22(6):351–362, 1954.
- [70] Richard J. Rossi. *Mathematical Statistics: An Introduction to Likelihood Based Inference*. Wiley, 2008.
- [71] Mark Fox. *Quantum optics: an introduction*. Oxford Master Series in Physics, 6. Oxford University Press, USA, 2006.

Appendix A

AOD datasheet



This image is a Zygo Intensity Map showing a surface with a series of parallel, diagonal ridges and valleys. The ridges are represented by bright, alternating diagonal lines, while the valleys are represented by dark, alternating diagonal lines. The overall pattern is rectangular and centered within a dark field.

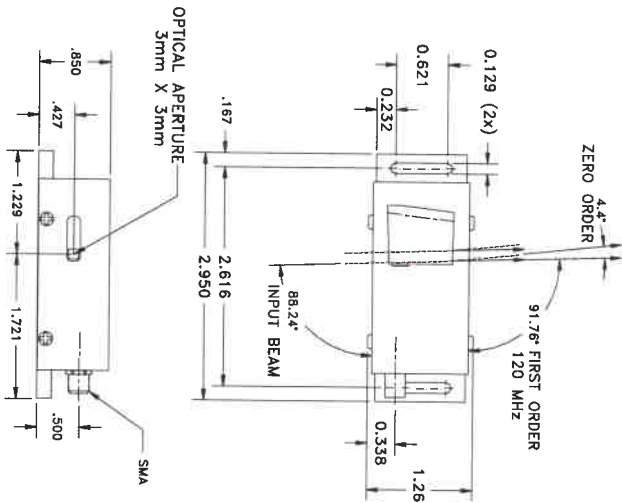
SPECIFICATIONS

AO Medium	TeO2
Acoustic Mode	Shear, off axis
Acoustic Velocity	.65 mm/μs
Wavelength	413 nm
Input Polarization	Horizontal
Output Polarization	Vertical
Insertion Loss	3%
Center Frequency (Fc)	120 MHz
RF Bandwidth	50 MHz
RF Power	<0.3 W
Active Aperture	3mm Diameter
Average Diffraction Efficiency	N/A
Flatness Across Bandwidth	N/A
Min Diffraction Efficiency	75%
Peak Valley at 633 mm	λ/4
RMS at 633 mm	N/A
VSWR	2.2:1
Scan Angle	N/A
Time Bandwidth	N/A

Notes:

- 1. First order @ 120MHz collinear to input +/- .45°
- 2. Impedance matching frequency range 80-145MHz

OUTLINE DRAWING



Document

09/13/13

Control

THIS DOCUMENT IS THE PROPERTY OF GOOCH & HOUSEGO. IT IS NOT TO BE REPRODUCED OR DISCLOSED IN WHOLE OR IN PART OTHER THAN BY EMPLOYEES OF GOOCH & HOUSEGO AND ITS CONTRACTED REPRESENTATIVES AND DISTRIBUTORS. ANY EXCEPTION REQUIRES THE WRITTEN CONSENT OF AN AUTHORIZED REPRESENTATIVE OF GOOCH & HOUSEGO.

TOLERANCES:
XX ± .01
XXX ± .005

DR 9/3/2013

DESCRIPTION:
AODF 4120-3
3MM APERTURE

MATERIAL:

CHK

APP

FINISH:

APP

PART NUMBER

97-02799-02

REV:

B

SHEET 1 OF 1

Appendix B

Polarization characterization

Here we report the figures for the polarization characterization of section ???. Every figure contains a fit of a sine function $A \sin(\omega x + \phi)$, where x is the angle of the corresponding waveplate. The fit are used to determine the maxima and minima of the curves which indicates the closest point to the desired polarization, see table ?? for results.

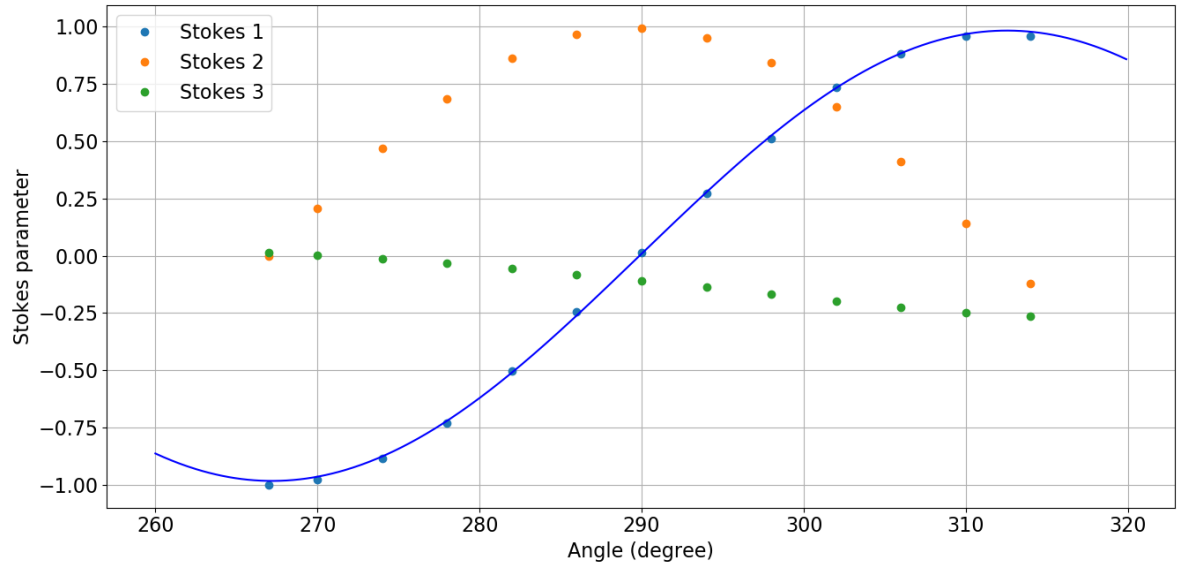


Figure B.0.1: Polarization after the $\lambda/2$ WP (see figure ??) as a function of the $\lambda/2$ WP B angle. Blue line is a sine function fit: $A = 0.983 \pm 0.007$, $\pi/\omega = 45.3 \pm 0.6^\circ$.

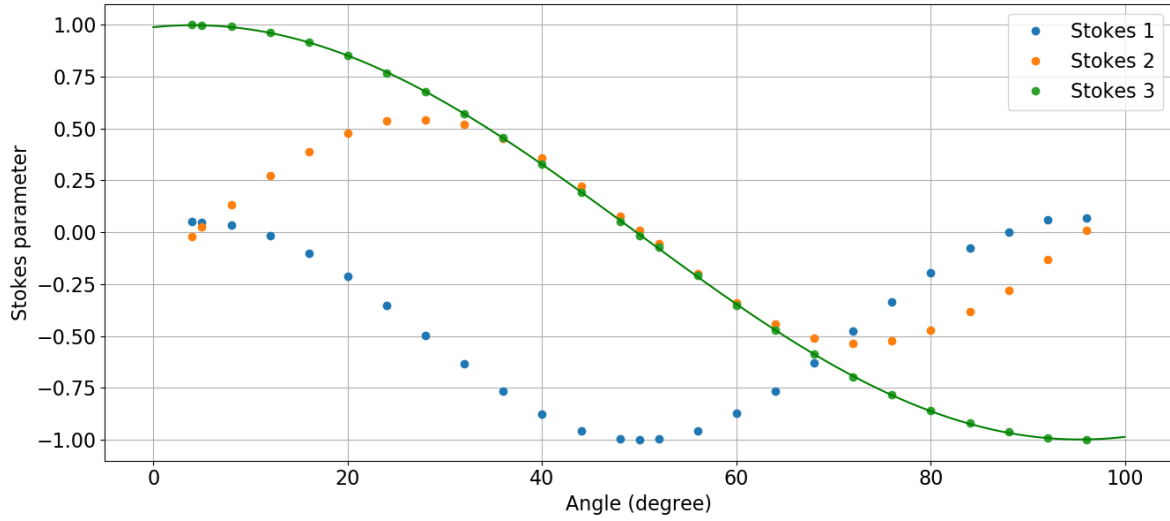


Figure B.0.2: Polarization after the objective at the focus spot as a function of the $\lambda/4$ angle with $\lambda/2$ WP B set to horizontal (267°). Green line is a sine function fit: $A = 0.998 \pm 0.02$, $\pi/\omega = 91.3 \pm 0.3^\circ$.

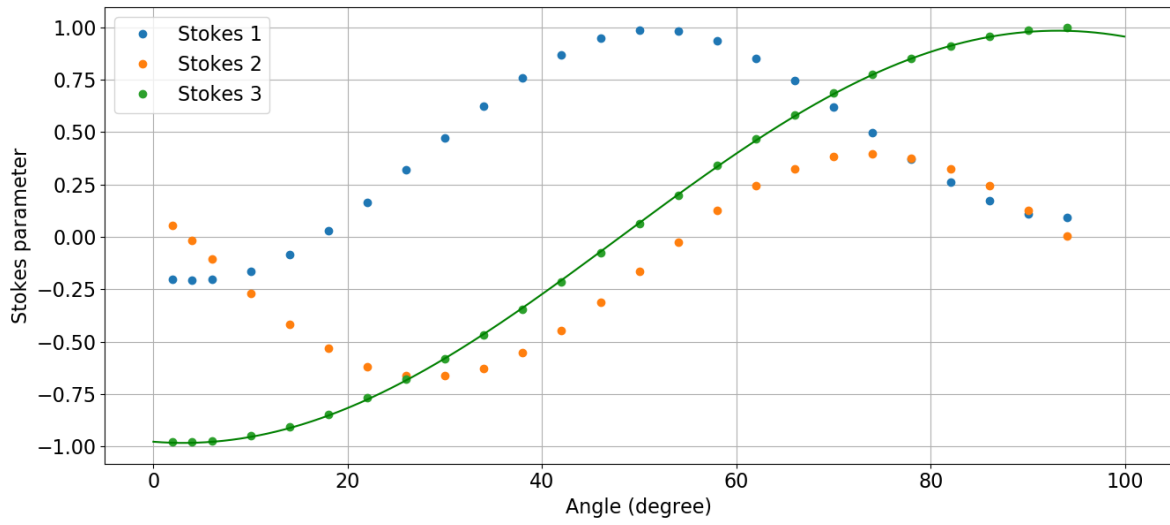


Figure B.0.3: Polarization after the objective at the focus spot as a function of the $\lambda/4$ angle with $\lambda/2$ WP B set to vertical (314°). Green line is a sine function fit: $A = 0.982 \pm 0.003$, $\pi/\omega = 90.0 \pm 0.5^\circ$.